Causal viscous hydrodynamics in 2 + 1 dimensions for relativistic heavy-ion collisions

Huichao Song[1,*] and Ulrich Heinz[1,2]
[1]*Department of Physics, Ohio State University, Columbus, Ohio 43210, USA*
[2]*CERN, Physics Department, Theory Division, CH-1211 Geneva 23, Switzerland*
(Received 21 December 2007; published 5 June 2008)

We explore the effects of shear viscosity on the hydrodynamic evolution and final hadron spectra of Cu + Cu collisions at ultrarelativistic collision energies, using the newly developed (2 + 1)-dimensional viscous hydrodynamic code VISH2+1. Based on the causal Israel-Stewart formalism, this code describes the transverse evolution of longitudinally boost-invariant systems without azimuthal symmetry around the beam direction. Shear viscosity is shown to decelerate the longitudinal and accelerate the transverse hydrodynamic expansion. For fixed initial conditions, this leads to a longer quark-gluon plasma (QGP) lifetime, larger radial flow in the final state, and flatter transverse momentum spectra for the emitted hadrons compared to ideal fluid dynamic simulations. We find that the elliptic flow coefficient v_2 is particularly sensitive to shear viscosity: even the lowest value allowed by the AdS/CFT conjecture $\eta/s \geqslant 1/4\pi$ suppresses v_2 enough to have significant consequences for the phenomenology of heavy-ion collisions at the BNL Relativistic Heavy Ion Collider (RHIC). A comparison between our numerical results and earlier analytic estimates of viscous effects within a blast-wave model parametrization of the expanding fireball at freeze-out reveals that the full dynamical theory leads to much tighter constraints for the specific shear viscosity η/s, thereby supporting the notion that the quark-gluon plasma created at RHIC exhibits almost "perfect fluidity."

DOI: 10.1103/PhysRevC.77.064901 PACS number(s): 25.75.Ld, 12.38.Mh, 24.10.Jv, 24.10.Nz

I. INTRODUCTION

Hydrodynamics is an efficient tool for describing the expansion of the fireballs generated in relativistic heavy-ion collisions. As a macroscopic description that provides the four-dimensional space-time evolution of the energy-momentum tensor $T^{\mu\nu}(x)$, it is much less demanding than microscopic descriptions based on kinetic theory that evolve the (on-shell) distribution function $f(x, p)$ in seven-dimensional phase space.

Ideal fluid dynamics is even more efficient since it reduces the number of independent fields needed to describe the symmetric energy-momentum tensor from 10 to 5: the local energy density $e(x)$, pressure $p(x)$, and the normalized flow four-velocity $u^\mu(x)$ (which has 3 independent components). The equation of state (EOS) $p(e)$ provides a further constraint which closes the set of four equations $\partial_\mu T^{\mu\nu}(x) = 0$.

Ideal fluid dynamics is based on the strong assumption that the fluid is in local thermal equilibrium and evolves isentropically. While local momentum isotropy in the co-moving frame is sufficient for a unique decomposition of the energy-momentum tensor in terms of e, p, and u^μ, it does not in general guarantee a unique relationship $p(e)$. Generically, the equation of state $p(e)$ (a key ingredient for closing the set of hydrodynamic equations) becomes unique only after entropy maximization, i.e. after a locally thermalized state, with Maxwellian (or Bose-Einstein and Fermi-Dirac) momentum distributions in the comoving frame, has been reached. For this assumption to be valid, the microscopic collision time scale must be much shorter than the macroscopic evolution time scale. Since the fireballs created in relativistic heavy-ion collisions are small and expand very rapidly, applicability of the hydrodynamic approach has long been doubted.

It came therefore as a surprise to many that the bulk of the matter produced in Au + Au collisions at the BNL Relativistic Heavy Ion Collider (RHIC) was found to behave as an almost ideal fluid. Specifically, ideal fluid dynamic models correctly reproduce the hadron transverse momentum spectra in central and semiperipheral collisions, including their anisotropy in noncentral collisions given by the elliptic flow coefficient $v_2(p_T)$ and its dependence on the hadron rest mass, for transverse momenta up to about 1.5–2 GeV/c [1], which covers more than 99% of the emitted particles. This observation has led to the conclusion that the quark-gluon plasma (QGP) created in RHIC collisions thermalizes very fast and must therefore be strongly (nonperturbatively) interacting [2], giving rise to the notion that the QGP is a strongly coupled plasma [3–5] that behaves as an almost perfect fluid.[1]

*Correspond to: song@mps.ohio-state.edu

[1]In an attempt to soften this conclusion it has been noted that the QGP is special in that for any gas of massless particles, the trace of the energy momentum tensor always vanishes (at least at the classical level) [6]. Local momentum isotropy is then indeed sufficient to ensure a unique relationship $e = 3p$ between energy density and pressure (EOS), irrespective of the particular form of the local (isotropic) momentum distribution. It has been suggested that this simple fact may extend the validity of ideal fluid dynamical descriptions to earlier times [6], after local momentum isotropy has already been reached but before complete thermalization, characterized by local entropy maximization, has been achieved [7–11]. This argument ignores, however, the observation from lattice QCD that quantum effects significantly violate the identity $e = 3p$ even in thermal equilibrium for temperatures up to about $2T_c$ (i.e., in the temperature regime probed by heavy-ion collisions at RHIC), and the

At RHIC energies, the almost perfect ideal fluid dynamical description of experimental data gradually breaks down in more peripheral collisions, at high transverse momenta, and at forward and backward rapidities; at lower energies, it lacks quantitative accuracy even in the most central collisions at midrapidity [12]. Most of these deviations from ideal fluid dynamical predictions can be understood as the result of strong viscous effects during the late hadronic stage of the fireball expansion [13] after the QGP has hadronized. As the initial energy density of the fireball decreases, the dissipative dynamics of the hadronic stage takes on increasing importance, concealing the perfect fluidity of any quark-gluon plasma possibly created at the beginning of the collision. However, as also pointed out in [13], persisting uncertainties about the initial conditions in heavy-ion collisions leave room for a small amount of viscosity even during the early QGP stage. Furthermore, the observed deviations of the elliptic flow parameter $v_2(p_T)$ at large p_T even in the largest collision systems at the highest available collision energies are consistent with viscous effects during the early epoch of the fireball [14,15]. During this epoch, the matter is so dense and strongly interacting that a microscopic description based on classical kinetic theory of on-shell partons [14] may be questionable. We therefore develop here a dissipative generalization of the macroscopic hydrodynamic approach, viscous relativistic fluid dynamics.

The need for such a framework is further highlighted by the recent insight that, due to quantum mechanical uncertainty [16], no classical fluid can have exactly vanishing viscosity (as is assumed in the ideal hydrodynamic approach). Even in the limit of infinitely strong coupling, the QGP must hence maintain a nonzero viscosity. Recent calculations of the shear viscosity to entropy ratio (the "specific shear viscosity" η/s) in a variety of conformal gauge field theories which share some properties with QCD, using the AdS/CFT correspondence, suggest a lower limit of $\frac{\eta}{s} = \frac{1}{4\pi}$ [17–19]. This is much smaller than the value obtained from weak coupling calculations in QCD [20] (although close to a recent first numerical result from lattice QCD [21]) and more than an order of magnitude below the lowest measured values in standard fluids [18]. Some alternative ideas of how small effective viscosities could be generated by anomalous effects (chaoticity) in anisotropically expanding plasmas [22] or by negative eddy viscosity in two-dimensional turbulent flows [23] have also been proposed.

Initial attempts to formulate relativistic dissipative fluid dynamics as a relativistic generalization of the Navier-Stokes equation [24,25] ran into difficulties because the resulting equations allowed for acausal signal propagation, and their solutions developed instabilities. These difficulties are avoided in the "second-order formalism" developed 30 years ago by Israel and Stewart [26] which expands the entropy current to second order in the dissipative flows and replaces the instantaneous identification of the dissipative flows with their driving forces multiplied by some transport coefficient (as is done in Navier-Stokes theory) by a kinetic equation that evolves the dissipative flows rapidly but smoothly toward their Navier-Stokes limit. This procedure eliminates causality and stability problems at the expense of numerical complexity: the dissipative flows become independent dynamical variables whose kinetic equations of motion are coupled and must be solved simultaneously with the hydrodynamic evolution equations. This leads effectively to more than a doubling of the number of coupled partial differential equations to be solved [27].

Only recently, computers have become powerful enough to allow efficient solution of the Israel-Stewart equations. The last 5 years have seen the development of numerical codes that solve these equations (or slight variations thereof [26–30]) numerically, for systems with boost-invariant longitudinal expansion and transverse expansion in zero [28,30], one [29,31–33], and two dimensions [34–37] (see also Ref. [38] for a numerical study of the relativistic Navier-Stokes equation in $2 + 1$ dimensions). The process of verification and validation of these numerical codes is still ongoing. While different initial conditions and evolution parameters used by the different groups of authors render a direct comparison of their results difficult, it seems unlikely that accounting for these differences will bring all the presently available numerical results in line with each other.

We here present results obtained with an independently developed $(2 + 1)$-dimensional causal viscous hydrodynamic code, VISH2+1.[2] While a short account of some of our main findings has already been published [36], we here report many more details, including extensive tests of the numerical accuracy of the code. We checked that (i) in the limit of vanishing viscosity, it accurately reproduces results obtained with the $(2 + 1)$-dimensional ideal fluid code AZHYDRO [39]; (ii) for homogeneous transverse density distributions (i.e. in the absence of transverse density gradients and transverse flow) and vanishing relaxation time, it accurately reproduces the known analytic solution of the relativistic Navier-Stokes equation for boost-invariant one-dimensional longitudinal expansion [40]; (iii) for very short kinetic relaxation times, our Israel-Stewart code accurately reproduces results from a separately coded $(2 + 1)$-dimensional relativistic Navier-Stokes code, under restrictive conditions where the latter produces numerically stable solutions; and (iv) for simple analytically parametrized anisotropic velocity profiles, the numerical code correctly computes the velocity shear tensor that drives the viscous hydrodynamic effects.

In its present early state, and given the existing open questions about the mutual compatibility of various numerical results reported in the recent literature, we believe that it is premature to attempt a detailed comparison of VISH2+1 with experimental data, in order to empirically constrain the specific shear viscosity of the QGP. Instead, we concentrate in this paper on describing and trying to understand the robustness of a variety of fluid dynamical effects generated by shear viscosity

novel fact, to be exposed later in this paper, that viscous effects caused by rapid longitudinal expansion at early times act *against* rapid local isotropization of the momentum distribution. Ideal hydrodynamics becomes valid only after these viscous effects have died away, and this happens sufficiently quickly only in strongly coupled plasmas.

[2]The acronym stands for "viscous Israel-Stewart hydrodynamics in $2 + 1$ space-time dimensions."

in a relativistic QGP fluid. We report here only results for Cu + Cu collisions, with initial entropy densities exceeding significantly those that can be reached in such collisions at RHIC. The reasons for doing so are purely technical. Initially our numerical grid was not large enough to accommodate Au + Au collision fireballs with sufficient resolution, and although this restriction has been lifted in the meantime, a large body of instructive numerical results had already been accumulated which would have been quite expensive to recreate for the Au + Au system. The unrealistic choice of initial conditions was driven by the wish to allow for a sufficiently long lifetime of the QGP phase even in peripheral Cu + Cu collisions such that shear viscous effects on elliptic flow would be still dominated by the quark-gluon plasma stage. The main goals of the present paper are to (i) quantitatively establish shear viscous effects on the evolution of the energy and entropy density, flow profile, source eccentricity, and total momentum anisotropy, on the final hadron spectra, and on the elliptic flow in central and noncentral heavy-ion collisions, under the influence of different equations of state; and (ii) explore in detail and explain physically how these effects arise, trying to extract general rules and generic features which should also apply for other collision systems and collision energies. We note that recent calculations for Au + Au collisions [41] have shown that viscous effects are somewhat bigger in the smaller Cu + Cu studied here than in the larger Au + Au system for which the largest body of experimental data exists. The reader must therefore apply caution when trying to compare (in his or her mind's eye) our results with the well-known RHIC Au + Au data.

The paper is organized as follows. Section II gives a brief review of the Israel-Stewart formalism for causal relativistic hydrodynamics for dissipative fluids, lists the specific form of these equations for the (2 + 1)-dimensional evolution of noncentral collision fireballs with boost-invariant longitudinal expansion which are solved by VISH2+1, and details the initial conditions and the equation of state (EOS) employed in our calculations. In Sec. III we report results for central ($b = 0$) Cu + Cu collisions. Section IV gives results for noncentral collisions, including a detailed analysis of the driving forces behind the strong shear viscous effects on elliptic flow observed by us. In Sec. V we explore the influence of different initializations and different relaxation times for the viscous shear pressure tensor on the hydrodynamic evolution and establish the limits of applicability for viscous hydrodynamics in the calculation of hadron spectra. Some technical details and the numerical tests performed to verify the accuracy of the computer code are discussed in Appendices A–D, and in Appendix E we compare our hydrodynamic results with analytical estimates of shear viscous effects by Teaney [15] that were based on Navier-Stokes theory and a blast-wave model parametrization of the fireball.

II. ISRAEL-STEWART THEORY OF CAUSAL VISCOUS HYDRODYNAMICS

In this section, we review briefly the second-order Israel-Stewart formalism for viscous relativistic hydrodynamics and the specific set of equations solved by VISH2+1 for anisotropic transverse expansion in longitudinally boost-invariant fireballs. Details of the derivation can be found in Ref. [27], with a small correction pointed out by Baier *et al.* in Ref. [30]. For simplicity, and in view of the intended application to RHIC collisions whose reaction fireballs have almost vanishing net baryon density, the discussion will be restricted to viscous effects, neglecting heat conduction and working in the Landau velocity frame [25].

A. Basics of Israel-Stewart theory

The general hydrodynamic equations arise from the local conservation of energy and momentum,

$$\partial_\mu T^{\mu\nu}(x) = 0, \tag{1}$$

where the energy-momentum tensor is decomposed in the form

$$T^{\mu\nu} = eu^\mu u^\nu - (p + \Pi)\Delta^{\mu\nu} + \pi^{\mu\nu}. \tag{2}$$

Here e and p are the local energy density and thermal equilibrium pressure, and u^μ is the (timelike and normalized, $u^\mu u_\mu = 1$) four-velocity of the energy flow. Π is the bulk viscous pressure; it combines with the thermal pressure p to the total bulk pressure. In Eq. (2) it is multiplied by the projector $\Delta^{\mu\nu} = g^{\mu\nu} - u^\mu u^\nu$ transverse to the flow velocity; i.e., in the local fluid rest frame, the bulk pressure is diagonal and purely spacelike, $(p + \Pi)\delta_{ij}$. $\pi^{\mu\nu}$ is the traceless shear viscous pressure tensor, also transverse to the four-velocity ($\pi^{\mu\nu}u_\nu = 0$) and thus purely spatial in the local fluid rest frame.

For ideal fluids, Π and $\pi^{\mu\nu}$ vanish, and the only dynamical fields are $e(x)$, $p(x)$, and $u^\mu(x)$, with e and p related by the equation of state $p(e)$. In dissipative fluids without heat conduction, Π and the five independent components of $\pi^{\mu\nu}$ enter as additional dynamical variables which require their own evolution equations. In relativistic Navier-Stokes theory, these evolution equations degenerate to instantaneous constituent equations,

$$\Pi = -\zeta\, \nabla\cdot u, \quad \pi^{\mu\nu} = 2\eta\, \nabla^{\langle\mu} u^{\nu\rangle}, \tag{3}$$

which express the *dissipative flows* Π and $\pi^{\mu\nu}$ directly in terms of their driving forces, the local expansion rate $\theta \equiv \nabla\cdot u$ and velocity shear tensor $\sigma^{\mu\nu} \equiv \nabla^{\langle\mu}u^{\nu\rangle}$, multiplied by phenomenological transport coefficients ζ, $\eta \geqslant 0$ (the bulk and shear viscosity, respectively). Here $\nabla^\nu \equiv \Delta^{\mu\nu}\partial_\nu$ is the gradient in the local fluid rest frame, and $\nabla^{\langle\mu}u^{\nu\rangle} \equiv \frac{1}{2}(\nabla^\mu u^\nu + \nabla^\nu u^\mu) - \frac{1}{3}(\nabla\cdot u)\Delta^{\mu\nu}$, showing that, like $\pi^{\mu\nu}$, the velocity shear tensor is traceless and transverse to u^μ. The instantaneous identification (3) leads to causality problems through instantaneous signal propagation, so that this straightforward relativistic generalization of the Navier-Stokes formalism turns out not to be a viable relativistic theory.

The Israel-Stewart approach [26] avoids these problems by replacing the instantaneous identifications (3) with the kinetic evolution equations

$$D\Pi = -\frac{1}{\tau_\Pi}\big(\Pi + \zeta\nabla\cdot u\big), \tag{4}$$

$$D\pi^{\mu\nu} = -\frac{1}{\tau_\pi}(\pi^{\mu\nu} - 2\eta\nabla^{\langle\mu}u^{\nu\rangle}) - (u^\mu\pi^{\nu\alpha} + u^\nu\pi^{\mu\alpha})Du_\alpha, \tag{5}$$

where $D = u^\mu\partial_\mu$ is the time derivative in the local fluid rest frame, and the last term in the bottom equation ensures that the kinetic evolution preserves the tracelessness and transversality of $\pi^{\mu\nu}$.[3] τ_Π and τ_π are relaxation times and related to the second-order expansion coefficients in the entropy current [26,28]. The fact that in the Israel-Stewart approach the dissipative flows Π and $\pi^{\mu\nu}$ no longer respond to the corresponding thermodynamic forces $\nabla\cdot u$ and $\nabla^{\langle\mu}u^{\nu\rangle}$ instantaneously, but on finite albeit short kinetic time scales, restores causality of the theory [26].

We should caution that the form of the kinetic evolution equations (4) and (5) is not generally agreed upon because of unresolved ambiguities in their derivation [26–31,34–37]. We will here use the form given in Eqs. (4) and (5) and comment on differences with other work when we discuss our results.

In the following calculations, we further simplify the problem by neglecting bulk viscosity. Bulk viscosity vanishes classically for a system of massless partons, and quantum corrections arising from the trace anomaly of the energy-momentum tensor are expected to be small, rendering bulk viscous effects much less important than those from shear viscosity. This expectation has been confirmed by recent lattice calculations [21,42] which yield very small bulk viscosity in the QGP phase. The same calculations show, however, a rapid rise of the bulk viscosity near the quark-hadron phase transition [42], consistent with earlier predictions [43,44]. In the hadronic phase, it is again expected to be small [43]. We leave the discussion of possible dynamical effects of bulk viscosity near the quark-hadron phase transition for a future study. Bulk viscous pressure effects can be easily restored by substituting $p \to p + \Pi$ everywhere below and adding the kinetic evolution equation (4) for Π.

[3]The last term in Eq. (5) does not contribute to entropy production and thus was missed in the derivation given in Ref. [27], which was based on an expansion of the entropy production rate to second order in the dissipative flows. Its importance for guaranteeing the preservation of tracelessness and transversality of $\pi^{\mu\nu}$ under kinetic evolution was pointed out in Ref. [30]. It happens to vanish identically for the case of azimuthally symmetric $(1+1)$-dimensional transverse expansion if one uses as independent dynamical fields those selected in Ref. [27] (namely, $\pi^{\eta\eta}$ and $\pi^{\phi\phi}$); hence these $(1+1)$-d equations preserve tracelessness and transversality automatically. The same is not true for the set of $(1+1)$-d evolution equations studied in Ref. [32], which instead of $\pi^{\eta\eta}$ evolves π^{rr}, and for azimuthally asymmetric transverse expansion in $2+1$ dimensions as discussed in the present paper, the last term in Eq. (5) must also be kept explicitly. (Note that this term was not included in Ref. [34], with unknown consequences.) We found that dropping the last term in Eq. (5) leads to problems with the velocity finding algorithm (see Appendix B), causing the code to crash after some time: as the shear pressure tensor evolves away from transversality to u^μ, the identity $e = T^{\tau\tau} - v_x T^{\tau x} - v_y T^{\tau y}$ [see Eq. (B1)] gets broken, leading eventually to unphysical solutions for e and [through Eqs. (B2) and (B3)] for the flow velocity.

B. Viscous hydrodynamics in 2 + 1 dimensions

In the present paper, we eliminate one of the three spatial dimensions by restricting our discussion to longitudinally boost-invariant systems. These are conveniently described in curvilinear $x^m = (\tau, x, y, \eta)$ coordinates, where $\tau = \sqrt{t^2 - z^2}$ is the longitudinal proper time, $\eta = \frac{1}{2}\ln(\frac{t+z}{t-z})$ is the space-time rapidity, and (x, y) are the usual Cartesian coordinates in the plane transverse to the beam direction z. In this coordinate system, the transport equations for the full energy momentum tensor $T^{\mu\nu}$ are written as [27]

$$\begin{aligned}
\partial_\tau\widetilde{T}^{\tau\tau} + \partial_x(v_x\widetilde{T}^{\tau\tau}) + \partial_y(v_y\widetilde{T}^{\tau\tau}) &= \mathcal{S}^{\tau\tau},\\
\partial_\tau\widetilde{T}^{\tau x} + \partial_x(v_x\widetilde{T}^{\tau x}) + \partial_y(v_y\widetilde{T}^{\tau x}) &= \mathcal{S}^{\tau x},\\
\partial_\tau\widetilde{T}^{\tau y} + \partial_x(v_x\widetilde{T}^{\tau y}) + \partial_y(v_y\widetilde{T}^{\tau y}) &= \mathcal{S}^{\tau y}.
\end{aligned} \tag{6}$$

Here $\widetilde{T}^{mn} \equiv \tau(T_0^{mn} + \pi^{mn})$, $T_0^{mn} = eu^m u^n - p\Delta^{mn}$ being the ideal fluid contribution, $u^m = (u^\tau, u^x, u^y, 0) = \gamma_\perp(1, v_x, v_y, 0)$ is the flow profile [with $\gamma_\perp = (\sqrt{1 - v_x^2 - v_y^2})^{-1}$], and $g^{mn} = \mathrm{diag}(1, -1, -1, -1/\tau^2)$ is the metric tensor for our coordinate system. The source terms $\mathcal{S}^{mn}$ on the right-hand side of Eq. (6) are given explicitly as

$$\begin{aligned}
\mathcal{S}^{\tau\tau} &= -p - \tau^2\pi^{\eta\eta} - \tau\partial_x(pv_x + \pi^{x\tau} - v_x\pi^{\tau\tau})\\
&\quad - \tau\partial_y(pv_y + \pi^{y\tau} - v_y\pi^{\tau\tau})\\
&\approx -p - \tau^2\pi^{\eta\eta} - \tau\partial_x(pv_x) - \tau\partial_y(pv_y), &(7)\\
\mathcal{S}^{\tau x} &= -\tau\partial_x(p + \pi^{xx} - v_x\pi^{\tau x}) - \tau\partial_y(\pi^{xy} - v_y\pi^{\tau x})\\
&\approx -\tau\partial_x(p + \pi^{xx}), &(8)\\
\mathcal{S}^{\tau y} &= -\tau\partial_x(\pi^{xy} - v_x\pi^{\tau y}) - \tau\partial_y(p + \pi^{yy} - v_y\pi^{\tau y})\\
&\approx -\tau\partial_y(p + \pi^{yy}). &(9)
\end{aligned}$$

We will see later (see the right panel of Fig. 13 below) that the indicated approximations of these source terms isolate the dominant drivers of the evolution and provide a sufficiently accurate quantitative understanding of its dynamics.

The transport equations for the shear viscous pressure tensor are

$$\begin{aligned}
&(\partial_\tau + v_x\partial_x + v_y\partial_y)\tilde{\pi}^{mn}\\
&\quad = -\frac{1}{\gamma_\perp\tau_\pi}(\tilde{\pi}^{mn} - 2\eta\tilde{\sigma}^{mn}) - \left(u^m\tilde{\pi}_j^n + u^n\tilde{\pi}_j^m\right)\\
&\qquad \times(\partial_\tau + v_x\partial_x + v_y\partial_y)u^j.
\end{aligned} \tag{10}$$

The expressions for $\tilde{\sigma}^{mn}$ and $\tilde{\pi}^{mn}$ are found in Eqs. (A1) and (A2); they differ from π^{mn} in Eqs. (7)–(9) and σ^{mn} given in Ref. [27] by a Jacobian τ^2 factor in the $(\eta\eta)$ component: $\tilde{\pi}^{\eta\eta} = \tau^2\pi^{\eta\eta}$, $\tilde{\sigma}^{\eta\eta} = \tau^2\sigma^{\eta\eta}$. This factor arises from the curved metric where the local time derivative $D = u^m d_m$ must be evaluated using covariant derivatives d_m.[4] Since $u^\eta = 0$, no such extra Jacobian terms arise in the derivative Du^j in the second line of Eq. (10).

The algorithm requires the propagation of $\pi^{\tau\tau}, \pi^{\tau x}, \pi^{\tau y}$, and $\pi^{\eta\eta}$ with Eq. (5), even though one of the first three

[4]This subtlety was overlooked in Eq. (5.6) of Ref. [27]; correspondingly, the left-hand sides of Eqs. (5.16a) and (5.21a) in Ref. [27] were written incorrectly. They should be corrected to read $\frac{1}{\tau^2}(\partial_\tau + v_x\partial_x + v_y\partial_y)(\tau^2\pi^{\eta\eta}) = \cdots$.

is redundant (see Ref. [36] and Appendix B). In addition, we have chosen to evolve several more, formally redundant components of π^{mn} using Eq. (5), and to use them for testing the numerical accuracy of the code, by checking that the transversality conditions $u_m\pi^{mn} = 0$ and the tracelessness $\pi^m_m = 0$ are preserved over time. We find them to be satisfied with an accuracy of better than 1–2% everywhere except for the fireball edge where the π^{mn} are very small and the error on the transversality and tracelessness constraints can become as large as 5%.

C. Initial conditions

For the ideal part $T_0^{\tau\tau}, T_0^{\tau x}, T_0^{\tau x}$ of the energy momentum tensor, we use the same initialization scheme as for ideal hydrodynamics. For simplicity and ease of comparison with previous ideal fluid dynamical studies, we here use a simple Glauber model initialization with zero initial transverse flow velocity where the initial energy density in the transverse plane is taken proportional to the wounded nucleon density [45]:

$$\begin{aligned} e_0(x,y;b) &= K n_{\mathrm{WN}}(x,y;b) \\ &= K\left\{T_A\left(x+\frac{b}{2},y\right)\left[1-\left(1-\frac{\sigma T_B\left(x-\frac{b}{2},y\right)}{B}\right)^B\right]\right. \\ &\quad \left. + T_B\left(x-\frac{b}{2},y\right)\left[1-\left(1-\frac{\sigma T_A\left(x+\frac{b}{2},y\right)}{A}\right)^A\right]\right\}. \end{aligned} \tag{11}$$

Here σ is the total inelastic nucleon-nucleon cross section, for which we take $\sigma = 40$ mb. $T_{A,B}$ is the nuclear thickness function of the incoming nucleus A or B, $T_A(x,y) = \int_{-\infty}^{\infty} dz \rho_A(x,y,z)$; $\rho_A(x,y,z)$ is the nuclear density given by a Woods-Saxon profile: $\rho_A(\boldsymbol{r}) = \frac{\rho_0}{1+\exp[(r-R_A)/\xi]}$. For Cu + Cu collisions, we take $R_{\mathrm{Cu}} = 4.2$ fm, $\xi = 0.596$ fm, and $\rho_0 = 0.17$ fm^{-3}. The proportionality constant K does not depend on collision centrality but on collision energy; it fixes the overall scale of the initial energy density and, via the associated entropy, the final hadron multiplicity to which it must be fitted as a function of collision energy. We here fix it to give $e_0 \equiv e(0,0;b=0) = 30$ GeV/fm^3 for the peak energy density in central Cu + Cu collisions, at an initial time τ_0 for the hydrodynamic evolution that we set as $\tau_0 = 0.6$ fm/c. As already mentioned in the Introduction, this exceeds the value reached in Cu + Cu collisions at RHIC (it would be appropriate for central Au + Au collisions at $\sqrt{s} = 200A$ GeV [1]). It ensures, however, a sufficiently long lifetime of the QGP phase in Cu + Cu collisions such that most of the final momentum anisotropy is generated during the QGP stage, thereby permitting a meaningful investigation of QGP viscosity on the elliptic flow generated in the collision.

Without a microscopic dynamical theory for the early preequilibrium stage, initializing the viscous pressure tensor π^{mn} requires some guess work. The effect of different choices for the initial π^{mn} on viscous entropy production during boost-invariant viscous hydrodynamic evolution without transverse expansion was recently studied in Ref. [46]. We will here explore two options: (i) we set $\pi_0^{mn} = 0$ initially [35]; or (ii) we assume that at time τ_0 one has $\pi_0^{mn} = 2\eta\sigma_0^{mn}$ where the shear tensor σ_0^{mn} is calculated from the initial velocity profile $u^m = (1,0,0,0)$ [32,34,37,38]. The second option is the default choice for most of the results shown in this paper. It gives $\tau^2\pi_0^{\eta\eta} = -2\pi_0^{xx} = -2\pi_0^{yy} = -\frac{4\eta}{3\tau_0}$, i.e., a negative contribution to the longitudinal pressure and a positive contribution to the transverse pressure.

We here present results for only one value of the specific shear viscosity, $\frac{\eta}{s} = \frac{1}{4\pi} \simeq 0.08$, corresponding to its conjectured lower limit [17]. The kinetic relaxation time τ_π will be taken as $\tau_\pi = \frac{3\eta}{sT}$ except were otherwise mentioned. This value is half the one estimated from classical kinetic theory for a Boltzmann gas of noninteracting massless partons [26,30]—we did not use the twice larger classical value because it led to uncomfortably large viscous pressure tensor components π^{mn} at early times, caused by large excursions from the Navier-Stokes limit. To study the sensitivity to different relaxation times and the approach to Navier-Stokes theory, we also performed a few calculations with $\tau_\pi = \frac{1.5\eta}{sT}$, which are presented in Sec. V B.

D. EOS

Through its dependence on the equation of state (EOS), hydrodynamic flow constitutes an important probe into the existence and properties of the quark-hadron phase transition which softens the EOS near T_c. To isolate effects induced by this phase transition from generic features of viscous fluid dynamics, we have performed calculations with two different equations of state, EOS I and SM-EOS Q. They are described in this subsection.

EOS I models a noninteracting gas of massless quarks and gluons, with $p = \frac{1}{3}e$. It has no phase transition. Where needed, the temperature is extracted from the energy density via the relation $e = (16 + \frac{21}{2}N_f)\frac{\pi^2}{30}\frac{T^4}{(\hbar c)^3}$, corresponding to a chemically equilibrated QGP with $N_f = 2.5$ effective massless quark flavors.

SM-EOS Q is a smoothed version of EOS Q [45] which connects a noninteracting QGP through a first-order phase transition to a chemically equilibrated hadron resonance gas. In the QGP phase, it is defined by the relation $p = \frac{1}{3}e - \frac{4}{3}B$ (i.e., $c_s^2 = \frac{\partial p}{\partial e} = \frac{1}{3}$). The vacuum energy (bag constant) $B^{1/4} = 230$ MeV is a parameter that is adjusted to yield a critical temperature $T_c = 164$ MeV. The hadron resonance gas below T_c can be approximately characterized by the relation $p = 0.15\,e$ (i.e., $c_s^2 = 0.15$) [45]. The two sides are matched through a Maxwell construction, yielding a relatively large latent heat $\Delta e_{\mathrm{lat}} = 1.15$ GeV/fm^3. For energy densities between $e_H = 0.45$ GeV/fm^3 and $e_Q = 1.6$ GeV/fm^3, one has a mixed phase with constant pressure (i.e., $c_s^2 = 0$). The discontinuous jumps of c_s^2 from a value of 1/3 to 0 at e_Q and back from 0 to 0.15 at e_H generate propagating numerical errors in VISH2+1 which grow with time and cause problems. We avoid these by smoothing the function $c_s^2(e)$ with a Fermi distribution of width $\delta e = 0.1$ GeV/fm^3 centered at $e = e_Q$ and another one of width $\delta e = 0.02$ GeV/fm^3 centered at

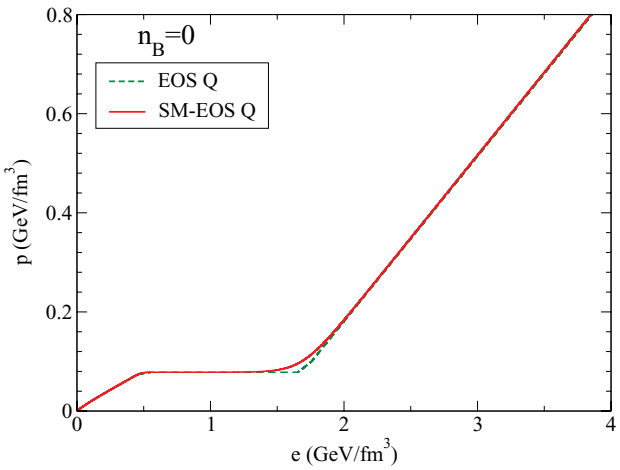

FIG. 1. (Color online) Equations of state EOS Q and SM-EOS Q (modified EOS Q).

$e = e_H$. Both the original EOS Q and our smoothed version SM-EOS Q are shown in Fig. 1. A comparison of simulations using ideal hydrodynamics with EOS Q and SM-EOS Q is given in Appendix D 1. It gives an idea of the magnitude of smoothing effects on the ideal fluid evolution of elliptic flow.

Another similarly smoothed EOS that matches a hadron resonance gas below T_c with lattice QCD data above T_c has also been constructed. Results using this lattice-based EOS will be reported elsewhere.

E. Freeze-out procedure: Particle spectra and v_2

Final particle spectra are computed from the hydrodynamic output via a modified Cooper-Frye procedure [47]. We here compute spectra only for directly emitted particles and do not include feeddown from resonance decay after freeze-out. We first determine the freeze-out surface $\Sigma(x)$ by postulating (as commonly done in hydrodynamic studies) that freeze-out from a thermalized fluid to free-streaming, noninteracting particles happens suddenly when the temperature drops below a critical value. As in the ideal fluid case with EOS Q [45] we choose $T_{\rm dec} = 130$ MeV. The particle spectrum is then computed as an integral over this surface, that is,

$$E\frac{d^3N_i}{d^3p} = \frac{g_i}{(2\pi)^3}\int_\Sigma p\cdot d^3\sigma(x) f_i(x,p) = \frac{g_i}{(2\pi)^3}\int_\Sigma p\cdot d^3\sigma(x)[f_{{\rm eq},i}(x,p)+\delta f_i(x,p)], \tag{12}$$

where g_i is the degeneracy factor for particle species i, $d^3\sigma^\mu(x)$ is the outward-pointing surface normal vector on the decoupling surface $\Sigma(x)$ at point x,

$$p\cdot d^3\sigma(x) = [m_T\cosh(y-\eta) - \boldsymbol{p}_\perp\cdot\nabla_\perp\tau_f(\boldsymbol{r})]\times\tau_f(\boldsymbol{r}) r\, dr d\phi d\eta \tag{13}$$

[with $\boldsymbol{r} = (x,y) = (r\cos\phi, r\sin\phi)$ denoting the transverse position vector], and $f_i(x,p)$ is the local distribution function for particle species i, computed from hydrodynamic output. Equation (12) generalizes the usual Cooper-Frye prescription for ideal fluid dynamics [47] by accounting for the fact that in a viscous fluid the local distribution function is never exactly in local equilibrium, but deviates from local equilibrium form by small terms proportional to the nonequilibrium viscous flows [15,30]. Both contributions can be extracted from hydrodynamic output along the freeze-out surface. The equilibrium contribution is

$$f_{{\rm eq},i}(p,x) = f_{{\rm eq},i}\left(\frac{p\cdot u(x)}{T(x)}\right) = \frac{1}{e^{p\cdot u(x)/T(x)}\pm 1}, \tag{14}$$

where the exponent is computed from the temperature $T(x)$ and hydrodynamic flow velocity $u^\mu = \gamma_\perp(\cosh\eta, v_\perp\cos\phi_v, v_\perp\sin\phi_v, \sinh\eta)$ along the surface $\Sigma(x)$:

$$p\cdot u(x) = \gamma_\perp[m_T\cosh(y-\eta) - p_T v_\perp\cos(\phi_p-\phi_v)]. \tag{15}$$

Here $m_T = \sqrt{p_T^2+m_i^2}$ is the particle's transverse mass. The viscous deviation from local equilibrium is given by [15,30]

$$\delta f_i(x,p) = f_{{\rm eq},i}(p,x)(1\mp f_{{\rm eq},i}(p,x))\frac{p^\mu p^\nu \pi_{\mu\nu}(x)}{2T^2(x)(e(x)+p(x))} \approx f_{{\rm eq},i}\cdot\frac{1}{2}\frac{p^\mu p^\nu}{T^2}\frac{\pi_{\mu\nu}}{e+p}. \tag{16}$$

The approximation in the second line is not used in our numerical results, but it holds (within the line thickness in all of our corresponding plots) since $(1\mp f_{\rm eq})$ deviates from unity only when $p \ll T$ where the last factor is small. With it, the spectrum (12) takes the instructive form

$$E\frac{d^3N_i}{d^3p} = \frac{g_i}{(2\pi)^3}\int_\Sigma p\cdot d^3\sigma(x) f_{{\rm eq},i}(x,p)\times\left(1+\frac{1}{2}\frac{p^\mu p^\nu}{T^2}\frac{\pi_{\mu\nu}}{e+p}\right). \tag{17}$$

The viscous correction is seen to be proportional to $\pi^{\mu\nu}(x)$ on the freeze-out surface (normalized by the equilibrium enthalpy $e+p$) and to increase quadratically with the particle's momentum (normalized by the temperature T). At large p_T, the viscous correction can exceed the equilibrium contribution, indicating a breakdown of viscous hydrodynamics. In that domain, particle spectra cannot be reliably computed with viscous fluid dynamics. The limit of applicability depends on the actual value of $\pi^{\mu\nu}/(e+p)$ and thus on the specific dynamical conditions encountered in the heavy-ion collision.

The viscous correction to the spectrum in Eq. (17) reads explicitly as

$$p_\mu p_\nu\pi^{\mu\nu} = m_T^2(\cosh^2(y-\eta)\pi^{\tau\tau} + \sinh^2(y-\eta)\tau^2\pi^{\eta\eta}) - 2m_T\cosh(y-\eta)(p_x\pi^{\tau x}+p_y\pi^{\tau y}) + \left(p_x^2\pi^{xx}+2p_xp_y\pi^{xy}+p_y^2\pi^{yy}\right). \tag{18}$$

We can use the expressions given in Appendix 2 of Ref. [27] in particular, Eqs. (A22) in that paper] to reexpress this in terms of the three independent components of π^{mn} for which we choose

$$\tilde\pi^{\eta\eta} = \tau^2\pi^{\eta\eta}, \quad \Sigma = \pi^{xx}+\pi^{yy}, \quad \Delta = \pi^{xx}-\pi^{yy}. \tag{19}$$

This choice is motivated by our numerical finding (see Fig. 2 in Ref. [36] and Sec. IV C) that $\tilde\pi^{\eta\eta}$, π^{xx}, and π^{yy} are about an

order of magnitude larger than all other components of π^{mn}, and that in the azimuthally symmetric limit of central ($b = 0$) heavy-ion collisions, the azimuthal average of Δ vanishes [see Eq. (C2)]: $\langle\Delta\rangle_\phi = 0$. We find

$$
\begin{aligned}
&p_\mu p_\nu \pi^{\mu\nu} \\
&\quad = \tilde{\pi}^{\eta\eta}\left[m_T^2(2\cosh^2(y-\eta)-1)\right. \\
&\qquad \left. -2\frac{p_T}{v_\perp}m_T\cosh(y-\eta)\frac{\sin(\phi_p+\phi_v)}{\sin(2\phi_v)}+\frac{p_T^2}{v_\perp^2}\frac{\sin(2\phi_p)}{\sin(2\phi_v)}\right] \\
&\qquad + \Sigma\left[m_T^2\cosh^2(y-\eta)-2\frac{p_T}{v_\perp}m_T\cosh(y-\eta)\right. \\
&\qquad \times\left(\frac{\sin(\phi_p+\phi_v)}{\sin(2\phi_v)}-\frac{v_\perp^2}{2}\frac{\sin(\phi_p-\phi_v)}{\tan(2\phi_v)}\right) \\
&\qquad \left. +\frac{p_T^2}{2}+\frac{p_T^2}{v_\perp^2}\left(1-\frac{v_\perp^2}{2}\right)\frac{\sin(2\phi_p)}{\sin(2\phi_v)}\right] \\
&\qquad + \Delta\left[p_T m_T\cosh(y-\eta)v_\perp\frac{\sin(\phi_p-\phi_v)}{\sin(2\phi_v)}\right. \\
&\qquad \left. -\frac{p_T^2}{2}\frac{\sin(2(\phi_p-\phi_v))}{\sin(2\phi_v)}\right]. \qquad (20)
\end{aligned}
$$

Because of longitudinal boost invariance, the integration over space-time rapidity η in Eq. (12) can be done analytically, resulting in a series of contributions involving modified Bessel functions [33,48]. VISH2+1 does not exploit this possibility and instead performs this and all other integrations for the spectra numerically.

Once the spectrum (12) has been computed, a Fourier decomposition with respect to the azimuthal angle ϕ_p yields the anisotropic flow coefficients. For collisions between equal spherical nuclei followed by longitudinally boost-invariant expansion of the collision fireball, only even-numbered coefficients contribute, the "elliptic flow" v_2 being the largest and most important one:

$$
\begin{aligned}
E\frac{d^3N_i}{d^3p}(b) &= \frac{dN_i}{dy p_T\, dp_T d\phi_p}(b) = \frac{1}{2\pi}\frac{dN_i}{dy p_T\, dp_T} \\
&\quad \times[1+2v_2(p_T;b)\cos(2\phi_p)+\cdots]. \qquad (21)
\end{aligned}
$$

In practice, it is evaluated as the $\cos(2\phi_p)$ moment of the final particle spectrum,

$$
v_2(p_T) = \langle\cos(2\phi_p)\rangle \equiv \frac{\int d\phi_p\,\cos(2\phi_p)\,\frac{dN}{dy\,p_T dp_T\,d\phi_p}}{\int d\phi_p\,\frac{dN}{dy\,p_T dp_T\,d\phi_p}}, \qquad (22)
$$

where, according to Eq. (12), the particle spectrum is a sum of a local equilibrium and a nonequilibrium contribution (to be indicated symbolically as $N = N_{\rm eq} + \delta N$).

III. CENTRAL COLLISIONS

A. Hydrodynamic evolution

Even without transverse flow initially, the boost-invariant longitudinal expansion leads to a nonvanishing initial stress tensor σ^{mn} which generates nonzero target values for three components of the shear viscous pressure tensor: $\tau^2\pi^{\eta\eta} = \frac{-4\eta}{3\tau_0}$, $\pi^{xx} = \pi^{yy} = \frac{2\eta}{3\tau_0}$. Inspection of the source terms in Eqs. (7)–(9) then reveals that the initially negative $\tau^2\pi^{\eta\eta}$ reduces the longitudinal pressure, thus reducing the rate of cooling due to work done by the latter, while the initially positive values of π^{xx} and π^{yy} add to the transverse pressure and accelerate the development of transverse flow in x and y directions. As the fireball evolves, the stress tensor σ^{mn} receives additional contributions involving the transverse flow velocity and its derivatives [see Eq. (A2)] which render an analytic discussion of its effects on the shear viscous pressure impractical.

Figure 2 shows what one gets numerically. Plotted are the source terms (7) and (8), averaged over the transverse plane with the energy density as weight function, as a function of

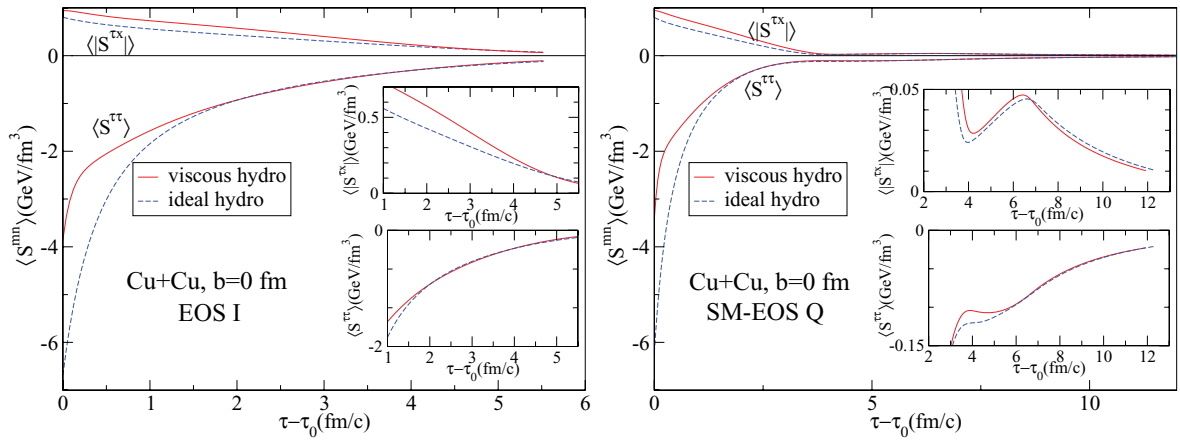

FIG. 2. (Color online) Time evolution of the hydrodynamic source terms in Eqs. (7)–(9), averaged over the transverse plane, for central Cu + Cu collisions, calculated with EOS I and SM-EOS Q. The small insets blow up the vertical scale to show more detail. The dashed blue lines are for ideal hydrodynamics with $e_0 = 30$ GeV/fm^3 and $\tau_0 = 0.6$ fm/c. Solid red lines show results from viscous hydrodynamics with identical initial conditions and $\frac{\eta}{s} = \frac{1}{4\pi} \approx 0.08$, $\tau_\pi = \frac{3\eta}{sT} \approx 0.24\left(\frac{200\,\text{MeV}}{T}\right)$ fm/c. The positive source terms drive the transverse expansion, while the negative ones affect the longitudinal expansion.

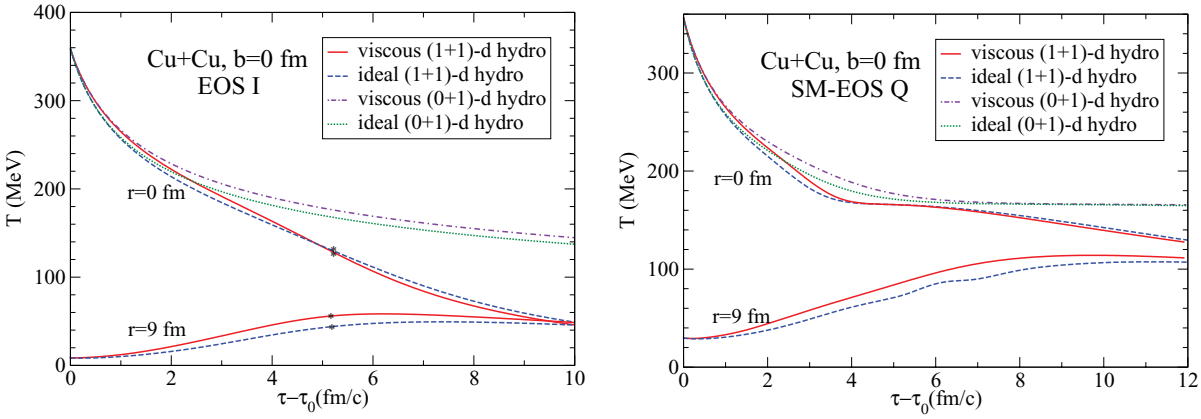

FIG. 3. (Color online) Time evolution of the local temperature in central Cu + Cu collisions, calculated with EOS I and SM-EOS Q, for the center of the fireball ($r = 0$) and a point near the edge ($r = 9$ fm). Same parameters as in Fig. 2.

time, for the evolution of central Cu + Cu collisions with two different equations of state, EOS I and SM-EOS Q. (In central collisions $\langle|\mathcal{S}^{\tau x}|\rangle = \langle|\mathcal{S}^{\tau y}|\rangle$.) One sees that the initially strong viscous reduction of the (negative) source term $\mathcal{S}^{\tau\tau}$, which controls the cooling by longitudinal expansion, quickly disappears. This is due to a combination of effects: while the magnitude of $\tau^2\pi^{\eta\eta}$ decreases with time, its negative effects are further compensated for by a growing positive contribution $\tau(\partial_x(pv_x) + \partial_y(pv_y))$ arising from the increasing transverse flow gradients. In contrast, the viscous increase of the (positive) transverse source term $\mathcal{S}^{\tau x}$ persists much longer, until about 5 fm/c. After that time, however, the viscous correction switches sign (clearly visible in the upper inset in the right panel of Fig. 2) and turns negative, thus reducing the transverse acceleration at late times relative to the ideal fluid case. We can summarize these findings by stating that shear viscosity reduces longitudinal cooling mostly at early times while causing initially increased but later reduced acceleration in the transverse direction. Because of the general smallness of the viscous pressure tensor components at late times, the last-mentioned effect (reduced acceleration) is not very strong.

The phase transition in SM-EOS Q is seen to cause an interesting nonmonotonic behavior of the time evolution of the source terms (right panel in Fig. 2), leading to a transient increase of the viscous effects on the longitudinal source term while the system passes through the mixed phase.

The viscous slowing of the cooling process at early times and the increased rate of cooling at later times due to accelerated transverse expansion are shown in Fig. 3. The upper set of curves shows what happens in the center of the fireball. For comparison we also show curves for boost-invariant longitudinal Bjorken expansion without transverse flow, labeled "(0 + 1)-d hydro". These are obtained with flat initial density profiles for the same value e_0 (no transverse gradients). The dotted green line in the left panel shows the well-known $T \sim \tau^{-1/3}$ behavior of the Bjorken solution of ideal fluid dynamics [49], modified in the right panel by the quark-hadron phase transition where the temperature stays constant in the mixed phase. The dash-dotted purple line shows the slower cooling in the viscous (0 + 1)-dimensional case [16], due to reduced work done by the longitudinal pressure. The expansion is still boost-invariant *á la* Bjorken [49] (as it is for all other cases discussed in this paper), but viscous effects generate entropy, thereby keeping the temperature at all times higher than for the adiabatic case. The dashed blue (ideal) and solid red (viscous) lines for the azimuthally

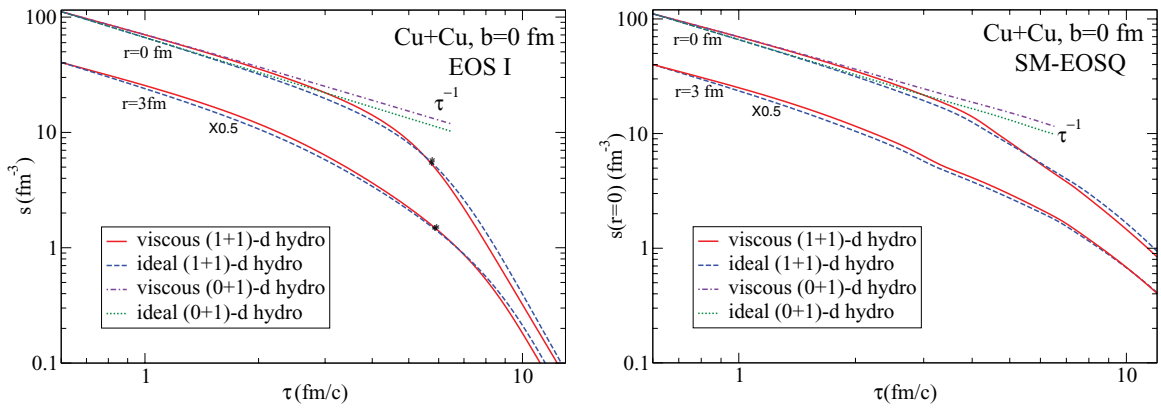

FIG. 4. (Color online) Time evolution of the local entropy density for central Cu + Cu collisions, calculated with EOS I and SM-EOS Q, for the center of the fireball ($r = 0$) and a point at $r = 3$ fm. Same parameters and color coding as in Fig. 3.

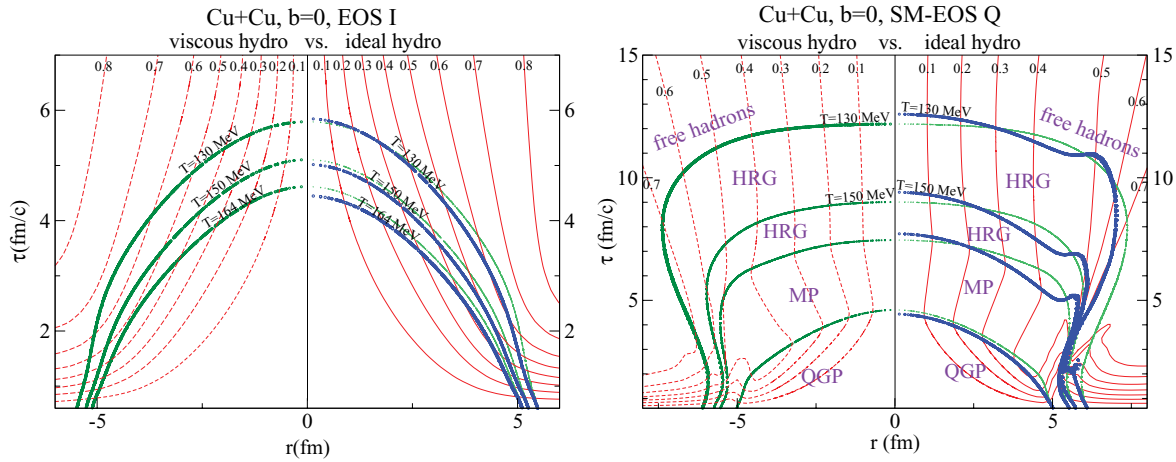

FIG. 5. (Color online) Surfaces of constant temperature T and constant transverse flow velocity $v_\perp$ for central Cu + Cu collisions, evolved with EOS I and SM-EOS Q. In each panel, results from viscous hydrodynamics in the left half are directly compared with the corresponding ideal fluid evolution in the right half. (The thin isotherm contours in the right halves of each panel are reflected from the left halves, for easier comparison.) The lines of constant $v_\perp$ are spaced by intervals of 0.1, from the inside outward, as indicated by the numbers near the top of the figures. The right panel contains two isotherms for $T_c = 164$ MeV, one separating the mixed phase (MP) from the QGP at energy density $e_Q = 1.6\,\mathrm{GeV/fm^3}$, the other separating it from the hadron resonance gas (HRG) at energy density $e_H = 0.45\,\mathrm{GeV/fm^3}$.[5] See text for discussion.

symmetric (1 + 1)-dimensional case show the additional cooling caused by transverse expansion. Again the cooling is initially slower in the viscous case, but at later times, due to faster buildup of transverse flow by the viscously increased transverse pressure, the viscous expansion is seen to cool the fireball center *faster* than ideal hydrodynamics. (Note also the drastic reduction of the lifetime of the mixed phase by transverse expansion; because of increased transverse flow and continued acceleration in the mixed phase from viscous pressure gradients, it is even more dramatic in the viscous than the ideal case.) The curves for $r = 9$ fm corroborate this, showing that the temperature initially increases with time due to hot matter being pushed from the center toward the edge, and that this temperature increase happens more rapidly in the viscous fluid because of the faster outward transport of matter in this case.

Figure 4 shows how the features seen in Fig. 3 manifest themselves in the evolution of the entropy density. (In the QGP phase, $s \sim T^3$.) The double-logarithmic presentation emphasizes the effects of viscosity and transverse expansion on the power law $s(\tau) \sim \tau^{-\alpha}$: one sees that the τ^{-1} scaling of the ideal Bjorken solution is flattened by viscous effects, but steepened by transverse expansion. As is well known, it takes a while (here about 3 fm/c) until the transverse rarefaction wave reaches the fireball center and turns the initially one-dimensional longitudinal expansion into a genuinely three-dimensional one. When this happens, the power law $s(\tau) \sim \tau^{-\alpha}$ changes from $\alpha = 1$ in the ideal fluid case to $\alpha > 3$ [1]. Here 3 is the dimensionality of space, and the fact that α becomes larger than 3 reflects relativistic Lorentz-contraction effects through the transverse-flow-related $\gamma_\perp$ factor that keeps increasing even at late times. In the viscous case, α changes from 1 to 3 sooner than for the ideal fluid because of the faster growth of transverse flow. At late times, the $s(\tau)$ curves for ideal and viscous hydrodynamics are almost perfectly parallel, indicating that very little entropy is produced during this late stage.

In Fig. 5, we plot the evolution of temperature in $r - \tau$ space, in the form of constant-T surfaces. Again, the two panels compare the evolution with EOS I to the one with SM-EOS Q. In the two halves of each panel, we directly contrast viscous and ideal fluid evolution. (The light gray lines in the right halves are reflections of the viscous temperature contours in the left halves, to facilitate comparison of viscous and ideal fluid dynamics.) Beyond the already noted fact that at $r = 0$, the viscous fluid cools initially more slowly (thereby giving somewhat longer life to the QGP phase) but later more rapidly (thereby freezing out earlier). This figure also exhibits two other noteworthy features. (i) Moving from $r = 0$ outward, one notes that contours of larger radial flow velocity are reached sooner in the viscous than in the ideal fluid case; this shows that radial flow builds up more quickly in the viscous fluid. This is illustrated more explicitly in Fig. 6, which shows the time evolution of the radial velocity $\langle v_\perp \rangle$, calculated as an average over the transverse plane with the Lorentz contracted energy density $\gamma_\perp e$ as the weight function. (ii) Comparing the two sets of temperature contours shown in the right panel of Fig. 5, one sees that viscous effects tend to smoothen any structures related to the (first order) phase transition in SM-EOS Q. The reason for this is that with the discontinuous change of the speed of sound at either end of the mixed phase, the radial flow velocity profile develops dramatic structures at the QGP-MP and MP-HRG interfaces [45].

[5]The structure at $\tau \sim 2$ fm/c and $r \sim 6$ fm in the $T = 130$ MeV ideal fluid isotherm for SM-EOS Q (also visible in the corresponding ideal fluid curves in Fig. 9) appears to be a numerical artifact that becomes less prominent when the numerical viscosity of the transport algorithm in AZHYDRO [39] is increased.

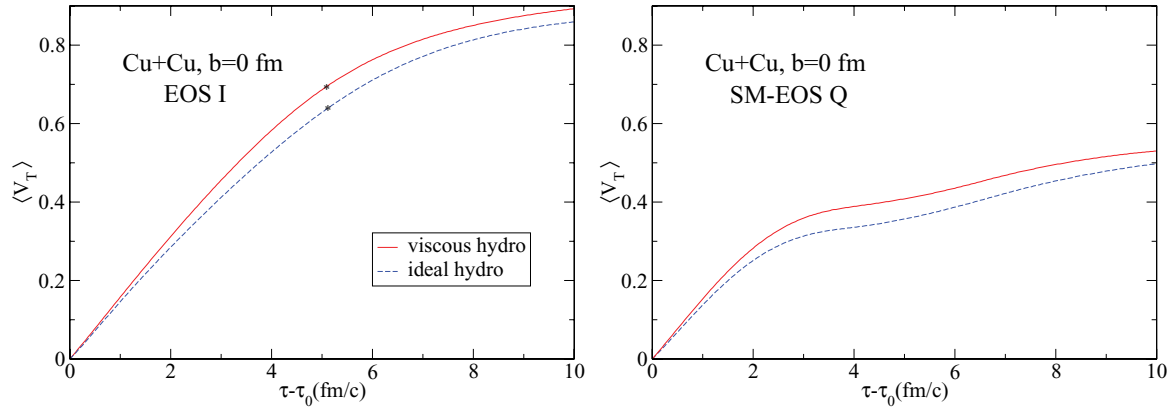

FIG. 6. (Color online) Time evolution of the average radial flow velocity $\langle v_T \rangle \equiv \langle v_\perp \rangle$ in central Cu + Cu collisions, calculated with EOS I and SM-EOS Q, comparing ideal and viscous fluid dynamics. The initially faster rate of increase reflects large positive shear viscous pressure in the transverse direction at early times. The similar rates of increase at late times indicate the gradual disappearance of shear viscous effects. In the right panel, the curves exhibit a plateau from 2 to 4 fm/c, reflecting the softening of the EOS in the mixed phase.

This leads to large velocity gradients across these interfaces (as can be seen in the right panel of Fig. 5 in its lower right corner, which shows rather twisted contours of constant radial flow velocity), inducing large viscous pressures which drive to reduce these gradients (as seen in lower left corner of that panel). In effect, shear viscosity softens the first-order phase transition into a smooth but rapid cross-over transition.

These same viscous pressure gradients cause the fluid to accelerate even in the mixed phase where all thermodynamic pressure gradients vanish (and where the ideal fluid therefore does not generate additional flow). As a result, the lifetime of the mixed phase is shorter in viscous hydrodynamics, as also seen in the right panel of Fig. 5.

B. Final particle spectra

After obtaining the freeze-out surface, we calculate the particle spectra from the generalized Cooper-Frye formula (12), using the AZHYDRO algorithm [39] for the integration over the freeze-out surface Σ. For calculations with EOS I, which lacks the transition from massless partons to hadrons, we cannot compute any hadron spectra. For illustration we instead compute the spectra of hypothetical massless bosons (gluons). They can be compared with the spectra from SM-EOS Q for pions, which can also, to good approximation, be considered as massless bosons.

The larger radial flow generated in viscous hydrodynamics, for a fixed set of initial conditions, leads, of course, to flatter transverse momentum spectra [29,32,33] at least at low p_T where the viscous correction δf_i to the distribution function can be neglected in Eq. (12)]. This is seen in Fig. 7, by comparing the dotted and solid lines. This comparison also shows that the viscous spectra lie systematically above the ideal ones, indicating larger final total multiplicity. This reflects the creation of entropy during the viscous hydrodynamic evolution. As pointed out in Refs. [32,33], this requires a retuning of initial conditions (starting the hydrodynamic evolution later with smaller initial energy density) if one desires to fit a given set of experimental p_T spectra. Since we here concentrate on investigating the origins and detailed mechanics of viscous effects in relativistic hydrodynamics, we will not explore

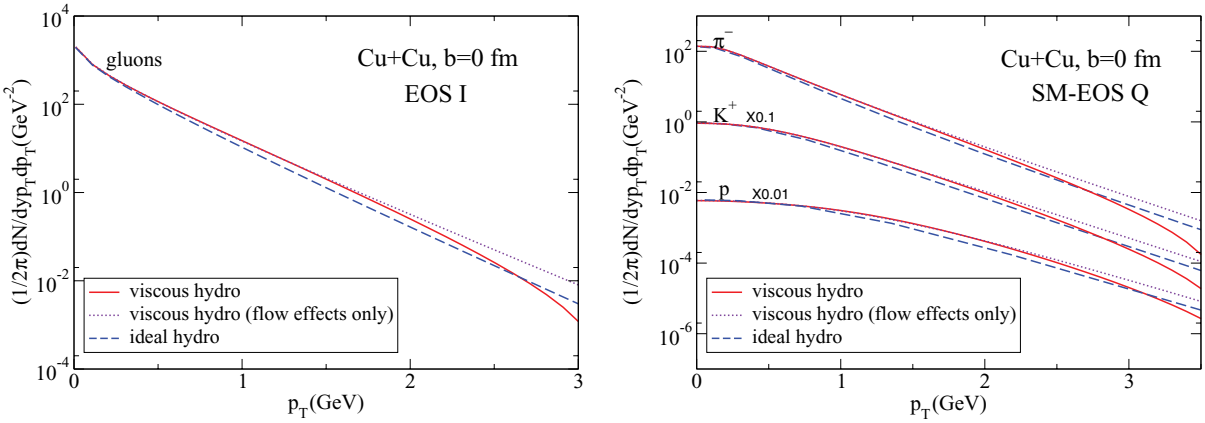

FIG. 7. (Color online) Midrapidity particle spectra for central Cu + Cu collisions, calculated with EOS I (gluons) and with SM-EOS Q (π^-, K^+, and p) for ideal and viscous hydrodynamics. The dotted lines show viscous hydrodynamic spectra that neglect the viscous correction δf_i to the distribution function in Eq. (12); i.e., they include only the effects from the larger radial flow generated in viscous hydrodynamics.

any variations of initial conditions. All comparisons between ideal and viscous hydrodynamics presented here use identical starting times τ_0 and initial peak energy densities e_0.

The viscous correction δf_i in Eqs. (12) and (16) depends on the signs and magnitudes of the various viscous pressure tensor components along the freeze-out surface, weighted by the equilibrium part $f_{\mathrm{eq},i}$ of the distribution function. Its effect on the final p_T spectra (even its sign!) is not *a priori* obvious. Teaney [15], using a blast-wave model to evaluate the velocity stress tensor $\sigma^{\mu\nu} = \pi^{\mu\nu}/(2\eta)$, found that the correction is positive, growing quadratically with p_T. Romatschke *et al.* [33,35] did not break out separately the contributions from larger radial flow in $f_{\mathrm{eq},i}$ and from δf_i. Dusling and Teaney [37], solving a slightly different set of viscous hydrodynamic equations and using a different (kinetic) freeze-out criterion to determine their decoupling surface, found a (small) positive effect from δf_i on the final pion spectra, at least up to $p_T = 2$ GeV/c, for freeze-out around $T_{\mathrm{dec}} \sim 130$ MeV, turning weakly negative when their effective freeze-out temperature was lowered to below 100 MeV. The dashed lines in Fig. 7 show that in our calculations for $p_T \gtrsim 2$ GeV/c, the effects from δf_i have an overall negative sign, leading to a reduction of the p_T spectra at large p_T relative to both the viscous spectra without δf_i and the ideal hydrodynamic spectra. This is true for all particle species, irrespective of the EOS used to evolve the fluid.

It turns out that when evaluating the viscous correction δf in Eq. (16) with the help of Eq. (20), large cancellations occur between the first and second line in Eq. (20). [After azimuthal integration, the contribution to δf from the third line $\sim \Delta$ vanishes identically for central collisions.] These cancellations cause the final result to be quite sensitive to small numerical errors in the calculation of $\tau^2\pi^{\eta\eta}$ and $\Sigma = \pi^{xx} + \pi^{yy}$. Increased numerical stability is achieved by trading $\tau^2\pi^{\eta\eta}$ for $\pi^{\tau\tau} = \tau^2\pi^{\eta\eta} + \Sigma$ and using instead of Eq. (20) the following expression:

$$
\begin{aligned}
& p_\mu p_\nu \pi^{\mu\nu} \\
&= \pi^{\tau\tau}\left[m_T^2(2\cosh^2(y-\eta)-1)\right. \\
&\quad \left. - 2\frac{p_T}{v_\perp} m_T \cosh(y-\eta)\frac{\sin(\phi_p+\phi_v)}{\sin(2\phi_v)} + \frac{p_T^2}{v_\perp^2}\frac{\sin(2\phi_p)}{\sin(2\phi_v)}\right] \\
&\quad + \Sigma\left[- m_T^2 \sinh^2(y-\eta) + p_T m_T \cosh(y-\eta) v_\perp \right. \\
&\quad \left. \times \frac{\sin(\phi_p-\phi_v)}{\tan(2\phi_v)} + \frac{p_T^2}{2}\left(1 - \frac{\sin(2\phi_p)}{\sin(2\phi_v)}\right)\right] \\
&\quad + \Delta\left[p_T m_T \cosh(y-\eta) v_\perp \frac{\sin(\phi_p-\phi_v)}{\sin(2\phi_v)}\right. \\
&\quad \left. - \frac{p_T^2}{2}\frac{\sin(2(\phi_p-\phi_v))}{\sin(2\phi_v)}\right]. \qquad (23)
\end{aligned}
$$

The first and second lines of this expression are now much smaller than before and closer in magnitude to the final net result for $p_\mu p_\nu \pi^{\mu\nu}$. This improvement carries over to noncentral collisions as discussed in Sec. IV D, where we also show the individual contributions from $\pi^{\tau\tau}$, Σ, and Δ to the particle spectra. To be able to use Eq. (23), the numerical code should directly evolve not only $\pi^{\tau\tau}$, $\pi^{\tau x}$, and $\pi^{\tau y}$, which are needed for the velocity-finding algorithm (see Appendix B), but also the components π^{xx} and π^{yy}. Otherwise, these last two components must be computed from the evolved π^{mn} components using the transversality and tracelessness constraints which necessarily involves the amplification of numerical errors by division with small velocity components.

In Fig. 8, we explore the nonequilibrium contribution to the final hadron spectra in greater detail. The figure shows that the nonequilibrium effects from δf_i are largest for massless particles and, at high p_T, decrease in magnitude with increasing particle mass. The assumption $|\delta f| \ll f_{\mathrm{eq}}$, which underlies the viscous hydrodynamic formalism, is seen to break down at high p_T, but to do so later for heavier hadrons than for lighter ones. Once the correction exceeds $\mathcal{O}(50\%)$ (indicated by the horizontal dashed line in Fig. 8), the calculated spectra can no longer be trusted.

In contrast to viscous hydrodynamics, ideal fluid dynamics has no intrinsic characteristic that will tell us when it starts to break down. Comparison of the calculated elliptic flow v_2 from ideal fluid dynamics with the experimental data from RHIC [1] suggests that the ideal fluid picture begins to break down above $p_T \simeq 1.5$ GeV/c for pions and above $p_T \simeq 2$ GeV/c for protons. This phenomenological hierarchy of thresholds where viscous effects appear to become essential is qualitatively consistent with the mass hierarchy from viscous hydrodynamics shown in Fig. 8.

In the region $0 < p_T \lesssim 1.5$ GeV/c, the interplay between m_T- and p_T-dependent terms in Eq. (20) is subtle, causing sign changes of the viscous spectral correction depending on hadron mass and p_T (see inset in Fig. 8). The fragility of the sign of the effect is also obvious from Fig. 8 in the work by Dusling and Teaney [37], where it is shown that in this p_T region the viscous correction changes sign from positive to negative when freeze-out is shifted from earlier to later times (higher to lower freeze-out temperature). Overall, we agree with them that the viscous correction effects on the p_T spectra

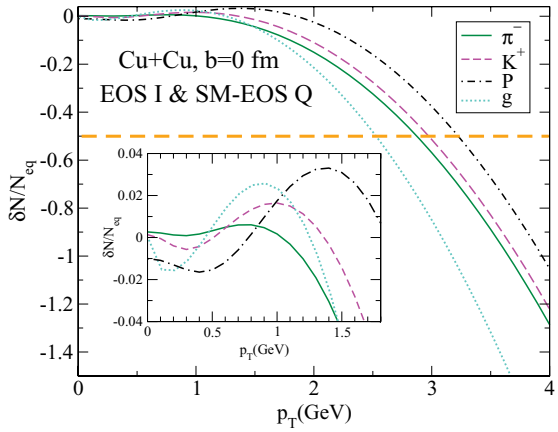

FIG. 8. (Color online) Ratio of the viscous correction δN, resulting from the nonequilibrium correction δf, Eq. (16), to the distribution function at freeze-out, to the equilibrium spectrum $N_{\mathrm{eq}} \equiv dN_{\mathrm{eq}}/(dy\, d^2p_T)$ calculated from Eq. (12) by setting $\delta f = 0$. The gluon curves are for evolution with EOS I, the curves for π^-, K^+, and p are from calculations with SM-EOS Q.

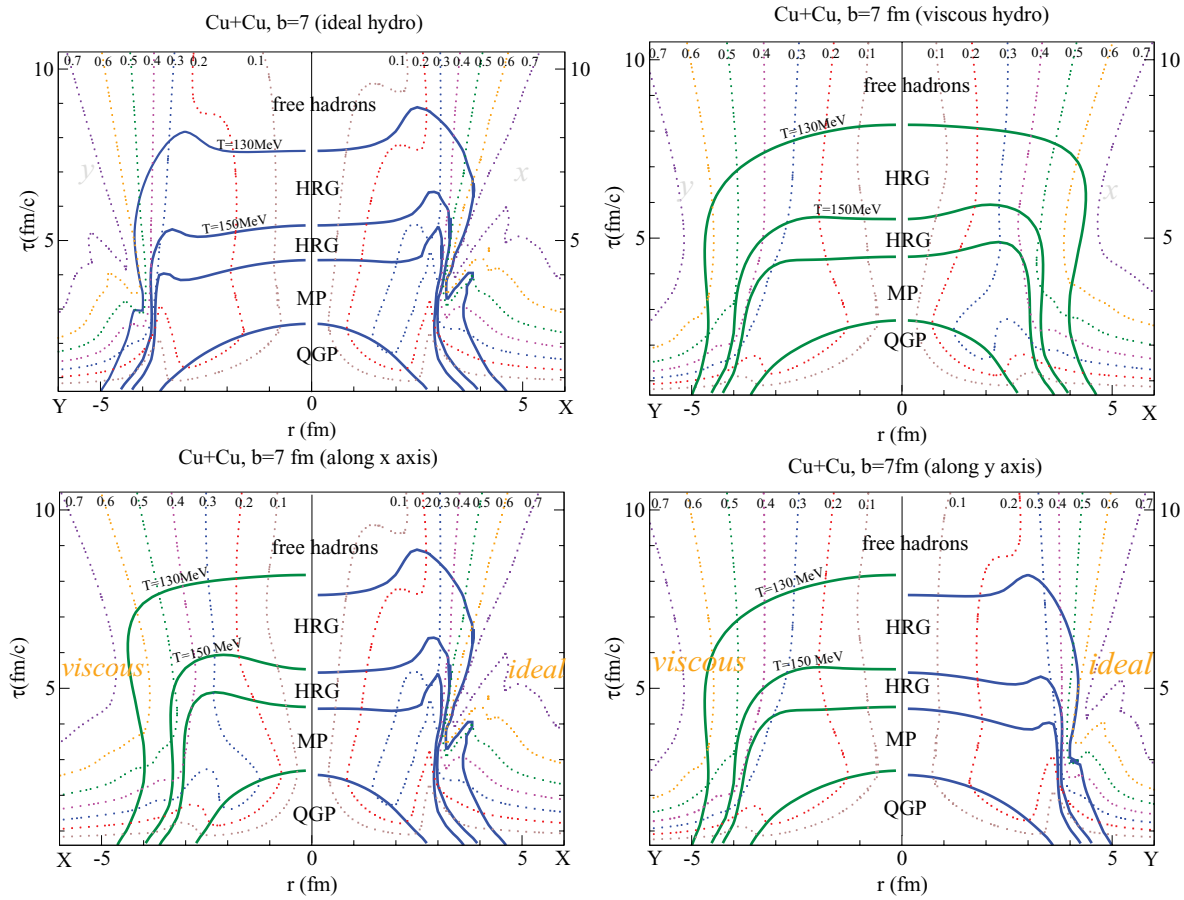

FIG. 9. (Color online) Surfaces of constant temperature T and constant transverse flow velocity $v_\perp$ for semiperipheral Cu + Cu collisions at $b = 7$ fm, evolved with SM-EOS Q. In the top row, we contrast ideal and viscous fluid dynamics, with a cut along the x axis (in the reaction plane) shown in the right half of each panel, while the left half shows a cut along the y axis (perpendicular to the reaction plane). In the bottom row, we compare ideal and viscous evolution in the each panel, with cuts along the x (y) direction shown in the left (right) panel. See Fig. 5 for comparison with central Cu + Cu collisions.[6]

are weak in this region [37]. We will see below that a similar statement does not hold for the elliptic flow.

IV. NONCENTRAL COLLISIONS

A. Hydrodynamic evolution

We now take full advantage of the ability of VISH2+1 to solve the transverse expansion in two spatial dimensions to explore the anisotropic fireball evolution in noncentral heavy-ion collisions. Similar to Fig. 5 for $b = 0$, Fig. 9 shows surfaces of constant temperature and radial flow for Cu + Cu collisions at $b = 7$ fm, for the equation of state SM-EOS Q. The plots show the different evolution into and perpendicular to the reaction plane and compare ideal with viscous fluid dynamics. Again, even a minimal amount of shear viscosity ($\frac{\eta}{s} = \frac{1}{4\pi}$) is seen to dramatically smoothen all structures related to the existence of a first-order phase transition in the EOS. However, in distinction to the case of central collisions, radial flow builds up at a weaker rate in the peripheral collisions and never becomes strong enough to cause faster central cooling at late times than seen in ideal fluid dynamics (bottom row in Fig. 9). The viscous fireball cools more slowly than the ideal one at all times and positions, lengthening in particular the lifetime of the QGP phase, and it grows to larger transverse size at freeze-out. Note that this does *not* imply larger transverse HBT radii than for ideal hydrodynamics (something that—in view of the "RHIC HBT puzzle" [1]–would be highly desirable): the larger geometric size is counteracted by larger radial flow such that the geometric growth, in fact, does not lead to larger transverse homogeneity lengths [33].

While Fig. 9 gives an impression of the anisotropy of the fireball in coordinate space, we study now in Fig. 10 the evolution of the flow anisotropy $\langle |v_x| - |v_y| \rangle$. In central collisions, this quantity vanishes. In ideal hydrodynamics, it is driven by the anisotropic gradients of the thermodynamic

[6]The structure at $\tau \sim 2$ fm/c and $r \sim 6$ fm in the $T = 130$ MeV ideal fluid isotherm for SM-EOS Q (also visible in the corresponding ideal fluid curves in Fig. 9) appears to be a numerical artifact that becomes less prominent when the numerical viscosity of the transport algorithm in AZHYDRO [39] is increased.

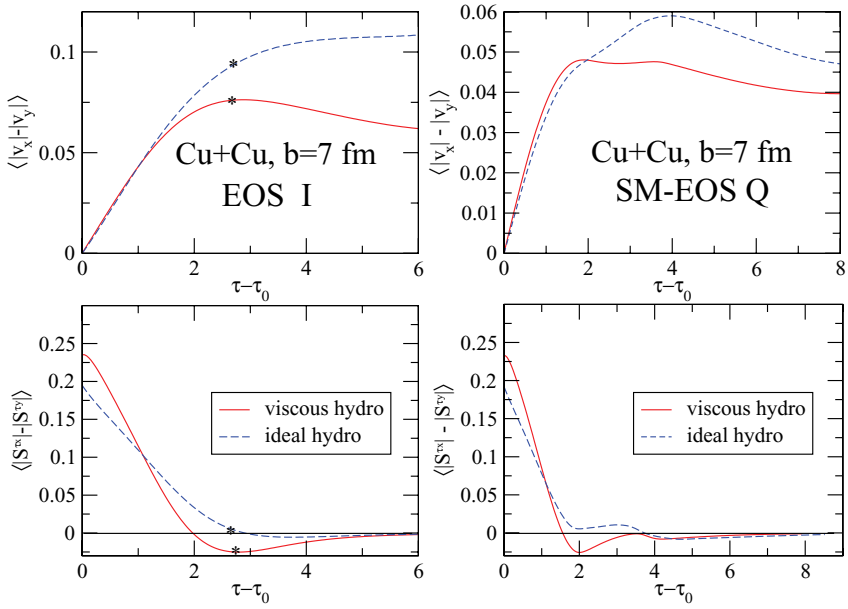

FIG. 10. (Color online) Time evolution of the transverse flow anisotropy $\langle |v_x| - |v_y| \rangle$ (top row) and of the anisotropy in the transverse source term $\langle |\mathcal{S}^{\tau x}| - |\mathcal{S}^{\tau y}| \rangle$ (bottom row). Both quantities are averaged over the transverse plane, with the Lorentz-contracted energy density $\gamma_\perp$ as weight function. The left (right) column shows results for EOS I (SM-EOS Q), comparing ideal and viscous fluid dynamical evolution.

pressure. In viscous fluid dynamics, the source terms of Eqs. (8) and (9), whose difference is shown in the bottom row of Fig. 10, receive additional contributions from gradients of the viscous pressure tensor which contribute their own anisotropies. Figure 10 demonstrates that these additional anisotropies *increase* the driving force for anisotropic flow at very early times ($\tau - \tau_0 < 1$ fm/c), but *reduce* this driving force throughout the later evolution. At times $\tau - \tau_0 > 2$ fm/c, the anisotropy of the effective transverse pressure even changes sign and turns negative, working to *decrease* the flow anisotropy. As a consequence of this, the buildup of the flow anisotropy stalls at $\tau - \tau_0 \approx 2.5$ fm/c (even earlier for SM-EOS Q, where the flow buildup stops as soon as the fireball medium enters the mixed phase) and proceeds to slightly decrease thereafter. This happens during the crucial period when ideal fluid dynamics still shows strong growth of the flow anisotropy. By the time the fireball matter decouples, the average flow velocity anisotropy of viscous hydrodynamics lags about 20–25% behind the value reached during ideal fluid dynamical evolution.

These features are mirrored in the time evolution of the spatial eccentricity $\epsilon_x = \frac{\langle x^2 - y^2 \rangle}{\langle x^2 + y^2 \rangle}$ [calculated by averaging over the transverse plane with the energy density $e(x)$ as weight function [45] and shown in the top row of Fig. 11] and of the momentum anisotropies ϵ_p and ϵ_p' (shown in the bottom row). The momentum anisotropy $\epsilon_p = \frac{\langle T_0^{xx} - T_0^{yy} \rangle}{\langle T_0^{xx} + T_0^{yy} \rangle}$ [50] measures the anisotropy of the transverse momentum density due to anisotropies in the collective flow pattern, as shown in top row of Fig. 10; it includes only the ideal fluid part of the energy momentum tensor. The *total momentum anisotropy* $\epsilon_p' = \frac{\langle T^{xx} - T^{yy} \rangle}{\langle T^{xx} + T^{yy} \rangle}$, similarly defined in terms of the total energy momentum tensor $T^{\mu\nu} = T_0^{\mu\nu} + \pi^{\mu\nu}$, additionally counts anisotropic momentum contributions arising from the viscous pressure tensor. Since the latter quantity includes effects due to the deviation δf of the local distribution function from its thermal equilibrium form which, according to Eq. (12), also affects the final hadron momentum spectrum and elliptic flow, it is this *total momentum anisotropy* that should be studied in viscous hydrodynamics if one wants to understand the evolution of hadron elliptic flow. In other words, in viscous hydrodynamics, hadron elliptic flow is not simply a measure for anisotropies in the collective flow velocity pattern, but additionally reflects anisotropies in the local rest frame momentum distributions, arising from deviations of the local momentum distribution from thermal equilibrium and thus being related to the viscous pressure.

Figure 11 correlates the decrease in time of the spatial eccentricity ϵ_x with the buildup of the momentum anisotropies ϵ_p and ϵ_p'. In viscous dynamics the spatial eccentricity is seen to decrease initially faster than for ideal fluids. This is less a consequence of anisotropies in the large viscous transverse pressure gradients at early times than a consequence of the faster radial expansion caused by their large overall magnitude. In fact, it was found a while ago [51] that for a system of free-streaming partons, the spatial eccentricity falls even faster than the viscous hydrodynamic curves (solid lines) in the upper row of Fig. 11. The effects of early pressure gradient anisotropies is reflected in the initial growth rate of the flow-induced momentum anisotropy ϵ_p, which is seen to slightly exceed that observed in the ideal fluid at times up to about 1 fm/c after the beginning of the transverse expansion (bottom panels in Fig. 11). This parallels the slightly faster initial rise of the flow velocity anisotropy seen in the top panels of Fig. 10. Figure 10 also shows that in the viscous fluid, the flow velocity anisotropy stalls about 2 fm/c after start and remains about 25% below the final value reached in ideal fluid

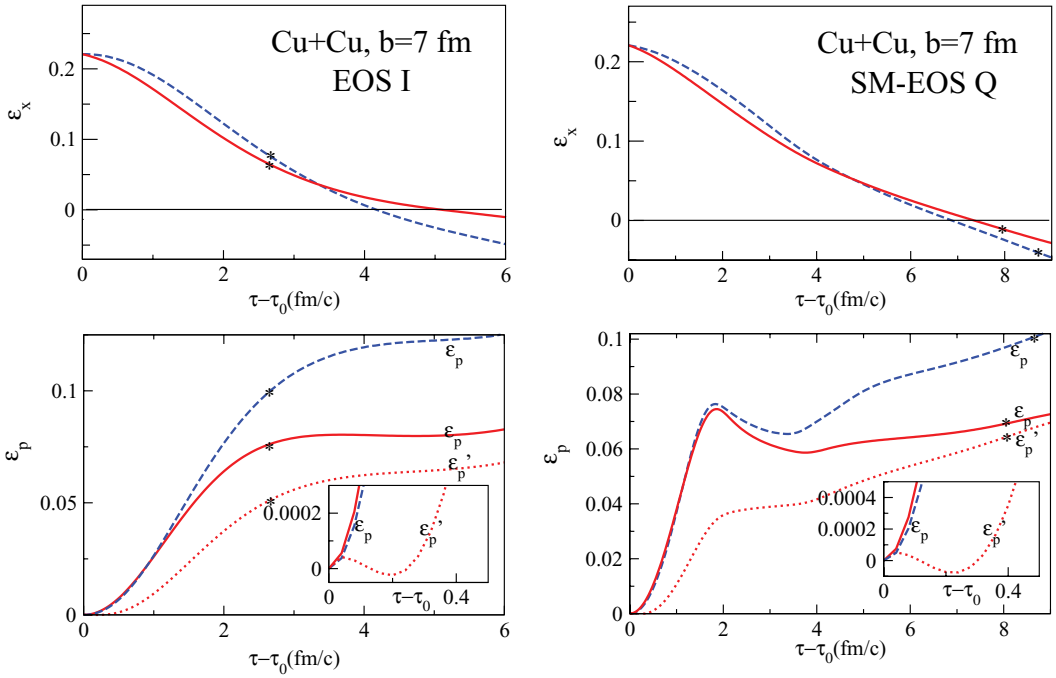

FIG. 11. (Color online) Time evolution for the spatial eccentricity ϵ_x, momentum anisotropy ϵ_p, and total momentum anisotropy ϵ_p' (see text for definitions), calculated for $b = 7$ fm Cu + Cu collisions with EOS I (left column) and SM-EOS Q (right column). Dashed lines are for ideal hydrodynamics, while the solid and dotted lines show results from viscous hydrodynamics.

dynamics. This causes the spatial eccentricity of the viscous fireball to decrease more slowly at later times than that of the ideal fluid (top panels in Fig. 11) which, at late times, features a significantly larger difference between the horizontal (x) and vertical (y) expansion velocities.

It is very instructive to compare the behavior of the flow-induced ideal-fluid contribution to the momentum anisotropy, ϵ_p, with that of the total momentum anisotropy ϵ_p'. At early times, they are very different, with ϵ_p' being much smaller than ϵ_p and even turning slightly *negative* at very early times (see insets in the lower panels of Fig. 11). This reflects very large *negative* contributions to the anisotropy of the total energy momentum tensor from the shear viscous pressure whose gradients along the out-of-plane direction y strongly exceed those within the reaction plane along the x direction. At early times, this effect almost compensates for the larger in-plane gradient of the thermal pressure. The *negative* viscous pressure gradient anisotropy is responsible for reducing the growth of flow anisotropies, thereby causing the flow-induced momentum anisotropy ϵ_p to significantly lag behind its ideal fluid value at later times. The negative viscous pressure anisotropies responsible for the difference between ϵ_p and ϵ_p' slowly disappear at later times, since all viscous pressure components then become very small (see Fig. 13 below).

The net result of this interplay is a total momentum anisotropy in Cu + Cu collisions (i.e., a source of elliptic flow v_2) that for a "minimally" viscous fluid with $\frac{\eta}{s} = \frac{1}{4\pi}$ is 40–50% lower than for an ideal fluid, at all except the earliest times (where it is even smaller). The origin of this reduction changes with time: initially it is dominated by strong momentum anisotropies in the local rest frame, with momenta pointing preferentially out-of-plane, induced by deviations from local thermal equilibrium and associated with large shear viscous pressure. At later times, the action of these anisotropic viscous pressure gradients integrates to an overall reduction in collective flow anisotropy, while the viscous pressure itself becomes small; at this stage, the reduction of the total momentum anisotropy is indeed mostly due to a reduced anisotropy in the collective flow pattern while momentum isotropy in the local fluid rest frame is approximately restored.

B. Elliptic flow v_2 of final particle spectra

The effect of the viscous suppression of the total momentum anisotropy ϵ_p' on the final particle elliptic flow is shown in Fig. 12. Even for the "minimal" viscosity $\frac{\eta}{s} = \frac{1}{4\pi}$ considered here, one sees a very strong suppression of the differential elliptic flow $v_2(p_T)$ from viscous evolution compared with the ideal fluid. Both the viscous reduction of the collective flow anisotropy (whose effect on v_2 is shown as the dotted lines) and the viscous contributions to the anisotropy of the local momentum distribution [embodied in the term δf in Eq. (12)] play big parts in this reduction. The runs with EOS I (which is a very hard EOS) decouple more quickly than those with SM-EOS Q; correspondingly, the viscous pressure components are still larger at freeze-out and the viscous corrections δf to the distribution function play a bigger role. With SM-EOS Q, the fireball does not freeze-out until π^{mn} has become very small (see Fig. 13 below), resulting in much smaller corrections

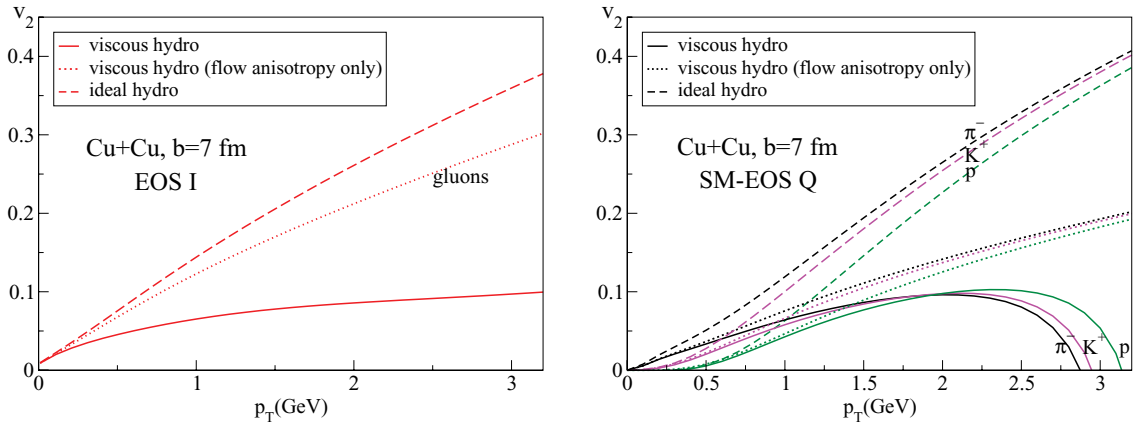

FIG. 12. (Color online) Differential elliptic flow $v_2(p_T)$ for Cu + Cu collisions at $b = 7$ fm.

from δf (difference between dashed and dotted lines in Fig. 12).[7] On the other hand, because of the longer fireball lifetime, the negatively anisotropic viscous pressure has more time to decelerate the buildup of anisotropic flow, so v_2 is strongly reduced because of the much smaller flow-induced momentum anisotropy ϵ_p.

The net effect of all this is that for Cu + Cu collisions and in the soft momentum region $p_T < 1.5$ GeV/c, the viscous evolution with $\frac{\eta}{s} = \frac{1}{4\pi}$ leads to a suppression of v_2 by about a factor 2,[8] in both the slope of its p_T dependence and its p_T-integrated value. [Because of the flatter p_T spectra from the viscous dynamics, the effect in the p_T-integrated v_2 is not quite as large as for $v_2(p_T)$ at fixed p_T.]

C. Time evolution of the viscous pressure tensor components and hydrodynamic source terms

In Fig. 13, we analyze the time evolution of the viscous pressure tensor components and the viscous hydrodynamic source terms on the right-hand side of Eq. (6). As already mentioned, the largest components of π^{mn} are $\tau^2\pi^{\eta\eta}$, π^{xx}, and π^{xy} (see Fig. 2 in Ref. [36] and left panel of Fig. 13).[9] At

[7]The right panel of Fig. 12 seems to indicate that $v_2(p_T)$ can even become negative at sufficiently large p_T—an observation first made in Ref. [15]. However, this only happens in the region where the viscous correction δf to the distribution function becomes comparable to or larger than the equilibrium contribution, so this feature cannot be trusted.

[8]Recently completed first simulations of Au + Au collisions indicate that the viscous suppression effects are not quite as big in this larger collision system as in the smaller Cu + Cu fireball studied here [41].

[9]Note that Fig. 2 in Ref. [36] shows averages over the entire 10 × 10 fm transverse grid used in VISH2+1, while the averages in our Figs. 13, 17, and 19 have been restricted to the thermalized region inside the freeze-out surface Σ. This eliminates a dependence of the average on the total volume covered by the numerical grid and more accurately reflects the relevant physics, since hydrodynamics applies only inside the decoupling surface.

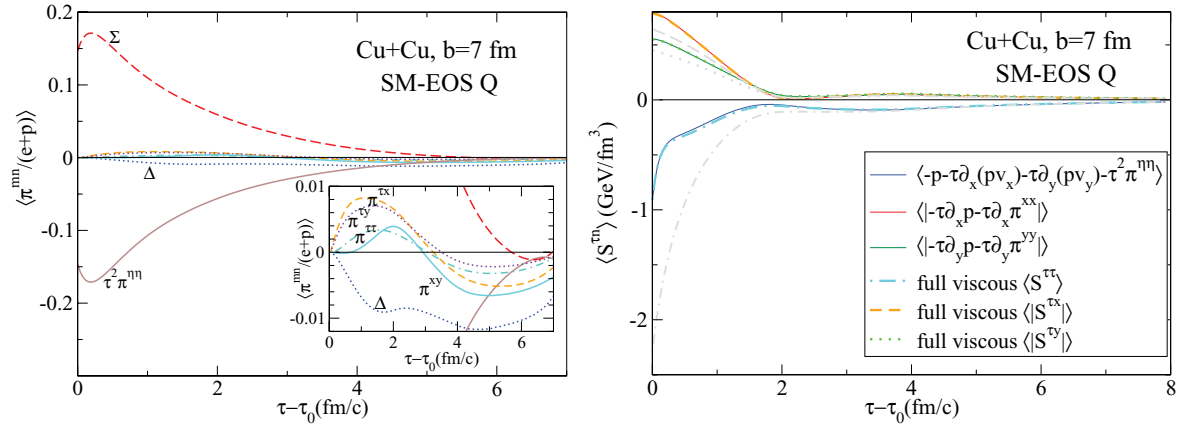

FIG. 13. (Color online) Left: Time evolution of the various components of the shear viscous pressure tensor, normalized by the enthalpy and averaged in the transverse plane over the thermalized region inside the freeze-out surface.Note that the normalizing factor $e + p \sim T^4$ decreases rapidly with time. Right: Comparison of the full viscous hydrodynamic source terms $\mathcal{S}^{mn}$, averaged over the transverse plane, with their approximations given in Eqs. (7)–(9), as a function of time. The thin gray lines indicate the corresponding source terms in ideal fluid dynamics.

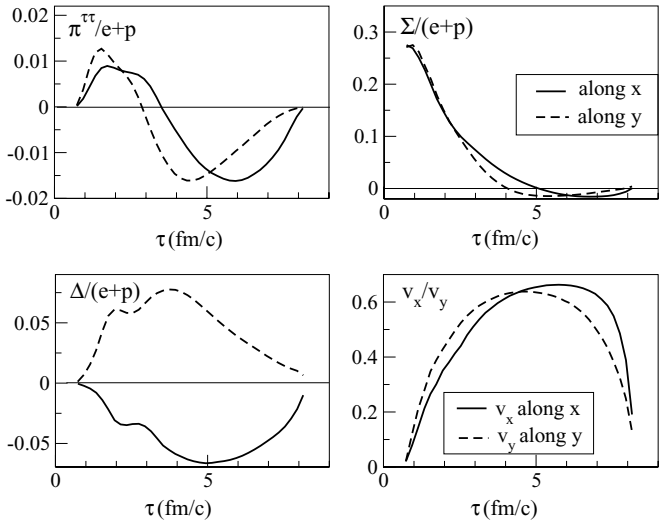

FIG. 14. Time evolution of $\pi^{\tau\tau}$, Σ, and Δ, as well as that of the transverse velocity, along the decoupling surface for $b = 7$ fm Cu + Cu collisions in viscous hydrodynamics with SM-EOS Q, as shown in Fig. 9. Solid and dashed lines represent cuts along, respectively, the x ($\phi = 0$) and y ($\phi = \frac{\pi}{2}$) directions.

early times, both $\tau^2\pi^{\eta\eta}$ and the sum $\Sigma = \pi^{xx} + \pi^{yy}$ reach (with opposite signs) almost 20% of the equilibrium enthalpy $e + p$. At this stage, all other components of π are at least an order of magnitude smaller (see inset). The largest of these small components is the difference $\Delta = \pi^{xx} - \pi^{yy}$, which we choose as the variable describing the anisotropy of the viscous pressure tensor in noncentral collisions. At late times ($\tau - \tau_0 > 5$ fm/c), when the large components of π^{mn} have strongly decreased, Δ becomes comparable to them in magnitude. As a fraction of the thermal equilibrium enthalpy $e + p \sim T^4$ which sets the scale in ideal fluid dynamics and which itself decreases rapidly with time, all viscous pressure components are seen to decrease with time. In a fluid with a set ratio η/s, viscous effects thus become less important with time. In real life, however, the ratio η/s depends itself on temperature and rises dramatically during the quark-hadron phase transition and below [52,53]. Shear viscous effects will therefore be larger at late times than considered here. The consequences of this will be explored elsewhere.

The observation that many components of π^{mn} are very small throughout the fireball evolution underlies the validity of the approximation of the hydrodynamic source terms given in the second lines of Eqs. (7)–(9). The excellent quality of this approximation is illustrated in the right panel of Fig. 13.

D. Viscous corrections to final pion spectra and elliptic flow

The large viscous reduction of the elliptic flow seen in Fig. 12 warrants a more detailed analysis of the viscous corrections to the particle spectra and v_2. In Fig. 14, we show, for Cu + Cu collisions at $b = 7$ fm evolved with SM-EOS Q, the time evolution of the independent components $\pi^{\tau\tau}$, Σ, and Δ of the viscous pressure tensor π^{mn}, normalized by the equilibrium enthalpy $e + p$, along the $T_{\rm dec} = 130$ MeV decoupling surface plotted in the upper right panel of Fig. 9. Solid (dashed) lines show the behavior along the x (y) direction [right (left) half of the upper right panel in Fig. 9]. We see that generically all three of these viscous pressure components are of similar magnitude, except for Σ which strongly dominates over the other two during the first 2 fm/c after the beginning of the expansion stage. However, since most particle production, especially that of low-p_T particles, occurs at late times ($\tau > 4$ fm/c for $b = 7$ fm/c Cu + Cu, see Fig. 9 and the discussion around Fig. 27 in Ref. [1]), the regions where Σ is large do not contribute much. As far as the nonequilibrium contribution to the spectra is concerned, we can thus say that the viscous pressure at freeze-out is of the order of a few percent of $e + p$. The anisotropy term Δ is even smaller because of cancellations between the in-plane (x) and out-of-plane (y) contributions when integrating over the azimuthal angle in Eq. (12).

These viscous pressure components generate the nonequilibrium contribution δf to the distribution function on the freeze-out surface according to Eqs. (16) and (23), resulting in a corresponding viscous correction to the azimuthally integrated particle spectrum $\delta N \equiv \int d\phi_p\, \delta(E\frac{d^3N}{d^3p})$. Figure 15 shows these nonequilibrium contributions for pions, normalized by the azimuthally averaged equilibrium part $N_{\rm eq} \equiv \int d\phi_p \frac{d^3N_{\rm eq}}{d^3p}$. We show both the total viscous correction and the individual contributions arising from the three independent pressure tensor components used in Eq. (23) and shown in Fig. 14.

In the viscous correction, the term from Eq. (23) [normalized by $T^2(e + p)$] is weighted by particle production via the equilibrium distribution function $f_{\rm eq}(x, p)$. It is well known (see Fig. 27 in Ref. [1]) that for low-p_T particles, this weight is concentrated along the relatively flat top part of the decoupling surface in Fig. 9, corresponding to $\tau \gtrsim 5 - 6$ fm/c in Fig. 14. In this momentum range, the contributions from $\pi^{\tau\tau}$, Σ, and Δ to $\delta N/N_{\rm eq}$ are of similar magnitude and alternating signs (see Fig. 15), making the sign of the overall viscous correction to the spectra hard to predict.

High-p_T particles, on the other hand, come from those regions in the fireball that feature the largest transverse flow velocity at freeze-out. Figure 9 shows that this restricts their emission mostly to the time interval $3 < \tau < 6$ fm/c. In this region, $\pi^{\tau\tau}$ is negative; see Fig. 14. A detailed study of the different terms in Eq. (23) reveals that (after azimuthal integration), the expression multiplying $\pi^{\tau\tau}$ is positive, hence the negative sign of $\pi^{\tau\tau}$ explains its negative contribution to $\delta N/N_{\rm eq}$ at high p_T, as seen in Fig. 15. Figure 15 also shows that in the region $p_T \gtrsim 1$ GeV/c the first line $\sim \pi^{\tau\tau}$ in Eq. (23) completely dominates the viscous correction to the spectra. We found that this involves additional cancellations between terms of opposite sign (after azimuthal integration) inside the square brackets multiplying Σ and Δ in the second and third lines of Eq. (23). Furthermore, the term $\sim \pi^{\tau\tau}$ is the only contribution whose magnitude grows quadratically with p_T. For the contributions involving Σ and Δ, the apparent quadratic momentum dependence seen in Eq. (23) is tempered by the integrations over space-time rapidity η and

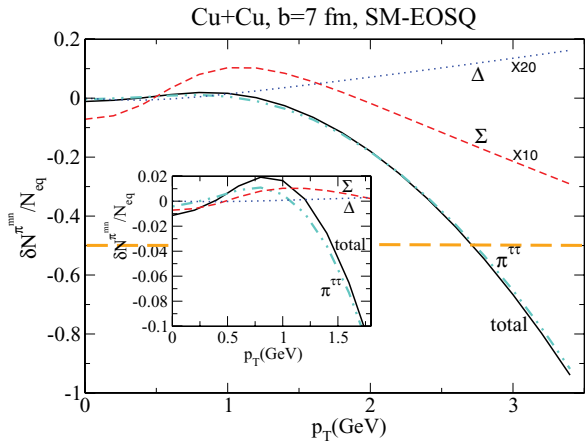

FIG. 15. (Color online) Viscous corrections to the azimuthally averaged pion spectrum resulting from individual components of the viscous pressure tensor π^{mn} as indicated, as well as the total correction $\delta N/N_{\rm eq}$, for Cu + Cu collisions at $b = 7$ fm with SM-EOS Q. The horizontal dashed line at -50% indicates the limit of validity.

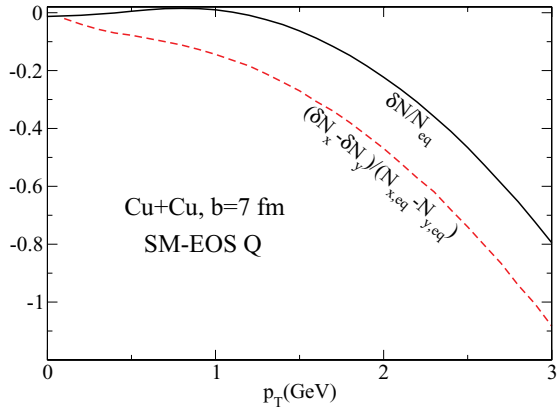

FIG. 16. (Color online) Ratio of nonequilibrium and equilibrium contributions to particle production (solid line) and to its momentum anisotropy (dashed line), as a function of p_T for pions from Cu + Cu collisions at $b = 7$ fm with SM-EOS Q.

azimuthal angle ϕ in Eq. (12), resulting in only linear growth at large p_T.

In the absence of higher order momentum anisotropies $v_n, n > 2$, the elliptic flow $v_2(p_T)$ can be easily computed from the momentum spectra in $x(\phi_p = 0)$ and $y(\phi_p = \frac{\pi}{2})$ directions:

$$2v_2(p_T) = \frac{N_x - N_y}{N} = \frac{(N_{x,\rm eq} - N_{y,\rm eq}) + (\delta N_x - \delta N_y)}{N_{\rm eq} + \delta N}, \tag{24}$$

where $N = N_{\rm eq} + \delta N$ is shorthand for the azimuthally averaged spectrum $dN/(2\pi\, dy\, p_T\, dp_T)$, and $N_{x,y}$ denote the p_T spectra along the x and y directions, respectively: $N_x \equiv N_{x,\rm eq} + \delta N_x \equiv \frac{d^3N}{dy\, p_T dp_T\, d\phi_p}(\phi_p = 0)$, and similarly for N_y with $\phi_p = \frac{\pi}{2}$. Equation (24) shows that v_2 receives contributions from anisotropies in the equilibrium part of the distribution function $f_{\rm eq}$, which reflect the hydrodynamic flow anisotropy along the freeze-out surface, and from the viscous correction δf, which reflects nonequilibrium momentum anisotropies in the local fluid rest frame. The dashed line in Fig. 16 shows the relative magnitude of these two anisotropy contributions, $\frac{\delta N_x - \delta N_y}{N_{x,\rm eq} - N_{y,\rm eq}}$, and compares it with the relative magnitude $\frac{\delta N}{N_{\rm eq}}$ of the nonequilibrium and equilibrium contributions to the total, ϕ_p-integrated pion spectrum for Cu + Cu at $b = 7$ fm. We see that the nonequilibrium contribution to the momentum anisotropy v_2 is always negative and larger in relative magnitude than the nonequilibrium contribution to the azimuthally averaged spectrum. Since v_2 is a small quantity reflecting the anisotropic distortion of the single-particle spectrum, it reacts more sensitively than the spectrum itself to the (anisotropic) nonequilibrium contributions caused by the small viscous pressure π^{mn} on the decoupling surface. Furthermore, the viscous corrections to the ϕ_p-integrated spectrum change sign as a function of p_T; the corrections to v_2 are negative everywhere, decreasing $v_2(p_T)$ at all values of p_T, but especially at large transverse momenta.

V. SENSITIVITY TO INPUT PARAMETERS AND LIMITS OF APPLICABILITY

A. Initialization of π^{mn}

Lacking input from a microscopic model of the pre-equilibrium stage preceding the (viscous) hydrodynamic one, one must supply initial conditions for the energy momentum tensor, including the viscous pressure π^{mn}. The most popular choice has been to initialize π^{mn} with its Navier-Stokes value, i.e., to set initially $\pi^{mn} = 2\eta\sigma^{mn}$. Up to this point, this has also been our choice in the present paper. Reference [35] advocated the choice $\pi^{mn} = 0$ at time τ_0 in order to minimize viscous effects and thus obtain an upper limit on η/s by comparison with experimental data. In the present section, we explore the sensitivity of the final spectra and elliptic flow to these different choices of initialization, keeping all other model parameters unchanged.

Figure 17 shows the time evolution of the viscous pressure tensor and viscous hydrodynamic source terms for the two different initializations. Differences with respect to the results shown in Fig. 13 (which are reproduced in Fig. 17 for comparison) are visible only at early times $\tau - \tau_0 \lesssim 5\tau_\pi \approx 1$ fm/c. After $\tau_\pi \sim 0.2$ fm/c, the initial difference $\pi^{mn} - 2\eta\sigma^{mn}$ has decreased by roughly a factor of $1/e$, and after several kinetic scattering times τ_π, the hydrodynamic evolution has apparently lost all memory of how the viscous terms were initialized.

Correspondingly, the final spectra and elliptic flow show very little sensitivity to the initialization of π^{mn}, as seen in Fig. 18. With vanishing initial viscous pressure, viscous effects on the final flow anisotropy are a little weaker (dotted lines in Fig. 18), but this difference is overcompensated in the total elliptic flow by slightly stronger anisotropies of the local rest frame momentum distributions at freeze-out (solid lines in Fig. 18). For shorter kinetic relaxation times τ_π, the differences resulting from different initializations of π^{mn} would be smaller still.

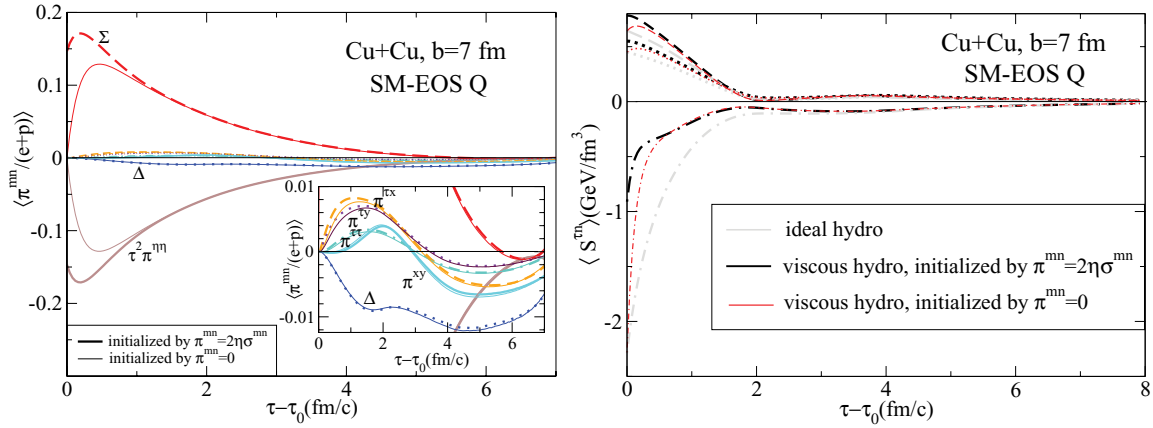

FIG. 17. (Color online) Similar to Fig. 13, but now comparing runs with different initial conditions. The thick lines reproduce the results from Fig. 13, obtained with $\pi^{mn} = 2\,\eta\sigma^{mn}$ at initial time τ_0, while thin lines of the same type show the corresponding results obtained by setting initially $\pi^{mn} = 0$. The right panel shows the full viscous source terms, without approximation: $\langle|\mathcal{S}^{\tau x}|\rangle$ (dashed), $\langle|\mathcal{S}^{\tau y}|\rangle$ (dotted), and $\langle\mathcal{S}^{\tau\tau}\rangle$ (dash-dotted).

B. Kinetic relaxation time τ_π

While the finite relaxation time τ_π for the viscous pressure tensor in the Israel-Stewart formalism eliminates problems with superluminal signal propagation in the relativistic Navier-Stokes theory, it also keeps the viscous pressure from ever fully approaching its Navier-Stokes limit $\pi^{mn} = 2\eta\sigma^{mn}$. In this section, we explore how far, on average, the viscous pressure evolved by VISH2+1 deviates from its Navier-Stokes limit, and how this changes if we reduce the relaxation time τ_π by a factor of 2.

In Fig. 19, we compare for central Cu + Cu collisions, the time evolution of the scaled viscous pressure tensor, averaged in the transverse plane over the thermalized region inside the freeze-out surface, with its Navier-Stokes limit, for two values of τ_π, that is, $\tau_\pi = 3\eta/sT = \tau_\pi^{\rm class}/2$ and $\tau_\pi = \tau_\pi^{\rm class}/4$. For the larger relaxation time, the deviations from the Navier-Stokes limit reach 25–30% at early times, but this fraction gradually decreases at later times. For the twice shorter relaxation time, the fractional deviation from Navier-Stokes decreases by somewhat more than a factor of 2 and never exceeds a value of about 10%.

Figure 20 shows that, small as they may appear, these deviations of π^{mn} from its Navier-Stokes limit $2\eta\sigma^{mn}$ (especially on the part of the decoupling surface corresponding to early times $\tau - \tau_0$) still play an important role in the viscous

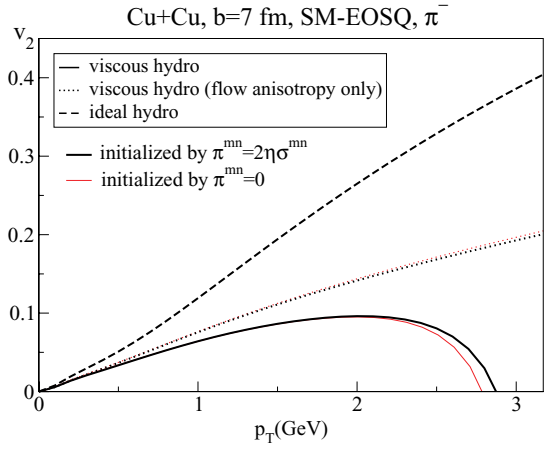

FIG. 18. (Color online) Differential elliptic flow $v_2(p_T)$ for pions from $b = 7$ fm Cu + Cu collisions with SM-EOS Q. Thick lines reproduce the pion curves from Fig. 12, obtained with $\pi^{mn} = 2\,\eta\sigma^{mn}$ at initial time τ_0, while thin lines of the same type show the corresponding results obtained by setting initially $\pi^{mn} = 0$.

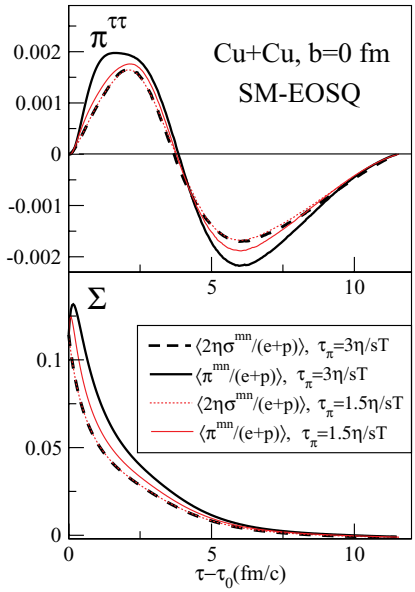

FIG. 19. (Color online) Time evolution of the two independent viscous pressure tensor components $\pi^{\tau\tau}$ and $\Sigma = \pi^{xx} + \pi^{yy}$ for central Cu + Cu collisions (solid lines), compared with their Navier-Stokes limits $2\eta\sigma^{\tau\tau}$ and $2\eta(\sigma^{xx} + \sigma^{yy})$ (dashed lines), for two values of the relaxation time, $\tau_\pi = 3\eta/sT$ (thick lines) and $\tau_\pi = 1.5\,\eta/sT$ (thin lines). All quantities are scaled by the thermal equilibrium enthalpy $e + p$ and transversally averaged over the thermalized region inside the decoupling surface.

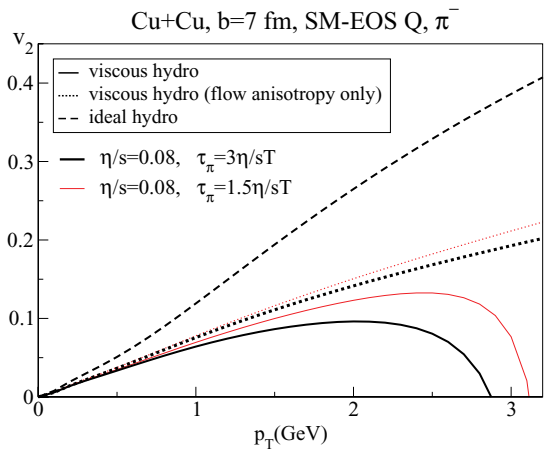

FIG. 20. (Color online) Differential elliptic flow $v_2(p_T)$ for π^- from $b = 7$ fm Cu + Cu collisions with SM-EOS Q, calculated from viscous hydrodynamics with two different values for the relaxation time τ_π. Thick lines reproduce the pion curves from Fig. 12, thin lines show results obtained with a twice shorter relaxation time. For the standard (twice larger) classical relaxation time value $\tau_\pi = 6\eta/sT$ [26,30] deviations from ideal hydrodynamics would exceed those seen in the thick lines.

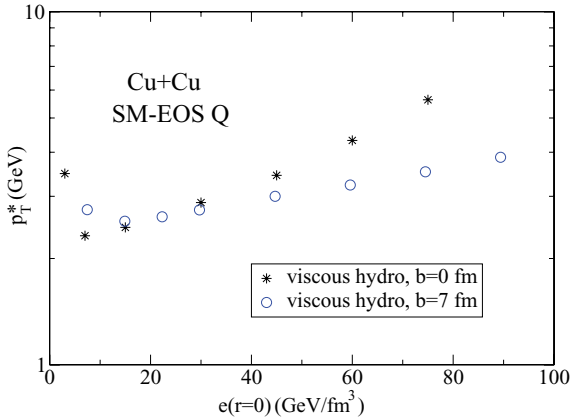

FIG. 21. (Color online) Characteristic transverse momentum p_T^* where the viscous corrections to the final pion spectrum become so large ($> 50\%$) that the spectrum becomes unreliable, as a function of the initial energy density in the center of the fireball. Stars are for central Cu + Cu collisions, open circles for peripheral Cu + Cu collisions at $b = 7$ fm. Note that identical $e(r = 0)$ values correspond to higher collision energies in peripheral than in central collisions. p_T^* values are higher for more massive hadrons (see Fig. 8), and they also increase for smaller relaxation times τ_π (see discussion of Fig. 20).

reduction of elliptic flow observed in our calculations. While a decrease of the relaxation time by a factor of 2 leads to only a small reduction of the viscous suppression of flow anisotropies (dotted lines in Fig. 20), the contribution to $v_2(p_T)$ resulting from the viscous correction $\sim p_m p_n \pi^{mn}$ to the final particle spectra is also reduced by about a factor of 2, leading to a significant overall increase of $v_2(p_T)$ in the region $p_T > 1$ GeV/c. To avoid strong sensitivity to the presently unknown value of the relaxation time τ_π in the QGP, future extractions of the specific shear viscosity η/s from a comparison between experimental data and viscous hydrodynamic simulations should therefore be performed at *low transverse momenta*, $p_T < 1$ GeV/c, where our results appear to be reasonably robust against variations of τ_π.

C. Breakdown of viscous hydrodynamics at high p_T

As indicated by the horizontal dashed lines in Figs. 8 and 15, the assumption $|\delta f| \ll |f_{\rm eq}|$ under which the viscous hydrodynamic framework is valid breaks down at sufficiently large transverse momenta. For a quantitative assessment, we assume that viscous hydrodynamic predictions become unreliable when the viscous corrections to the particle spectra exceed 50%. Figure 8 shows that the characteristic transverse momentum p_T^* where this occurs depends on the particle species and increases with particle mass. To be specific, we here consider p_T^* for pions—the values for protons would be about 15% higher. The discussion in the preceding section of the τ_π dependence of viscous corrections to the final spectra makes it clear that reducing τ_π will also push p_T^* to larger values. Since we do not know τ_π, we refrain from a quantitative estimate of this effect.

In Fig. 21, we show the breakdown momentum p_T^* for pions as a function of the peak initial energy density in the fireball center (i.e., indirectly as a function of collision energy), for both central and peripheral Cu + Cu collisions. (The initial time was held fixed at $\tau_0 = 0.6$ fm.) Generically, p_T^* rises with collision energy. The anomaly at low values of $e(r = 0)$ results, as far as we could ascertain, from effects connected with the phase transition in SM-EOS Q. The rise of p_T^* with increasing $e(r = 0)$ reflects the growing fireball lifetime which leads to smaller viscous pressure components at freeze-out. This lifetime effect is obviously stronger for central than for peripheral collisions, leading to the faster rise of the stars than the open circles in Fig. 21. Taking further into account that a given beam energy leads to higher $e(r = 0)$ values in central than in peripheral collisions such that, for a given experiment, the peripheral collision points are located farther to the left in the figure than the central collision points, we conclude that in central collisions, the validity of viscous hydrodynamics extends to *significantly larger* values of p_T than in peripheral collisions: viscous effects are more serious in peripheral than in central collisions.

VI. SUMMARY AND CONCLUSIONS

In this paper, we numerically studied the shear viscous effects on the hydrodynamic evolution, final hadron spectra, and elliptic flow v_2, using a (2 + 1)-dimensional causal viscous hydrodynamic code, VISH2+1, based on the second-order Israel-Stewart formalism. Using a fixed set of initial and final conditions, we explored the effects of shear viscosity for a "minimally" [18] viscous fluid with $\frac{\eta}{s} = \frac{1}{4\pi}$ in central and peripheral Cu + Cu collisions, comparing the evolution with two different equations of state, an ideal massless parton gas (EOS I) and an EOS with a semirealistic parametrization of the quark-hadron phase transition (SM-EOS Q). Final

hadron spectra and their elliptic flow were calculated from the hydrodynamic output using the Cooper-Frye prescription.

We found that shear viscosity decelerates longitudinal expansion but accelerates the build-up of transverse flow. This slows the cooling process initially, leading to a longer lifetime for the QGP phase, but causes accelerated cooling at later stages by faster transverse expansion. Viscous pressure gradients during the mixed phase increase the acceleration during this stage and slightly reduce its lifetime. They counteract large gradients of the radial velocity profile that appear in ideal fluid dynamics as a result of the softness of the EOS in the mixed phase, thereby *de facto* smoothing the assumed first-order phase transition into a rapid cross-over transition. In the end, the larger radial flow developing in viscous hydrodynamics leads to flatter transverse momentum spectra of the finally emitted particles, while their azimuthal anisotropy in noncentral heavy-ion collisions is found to be strongly reduced.

Although the viscous hardening of the hadron p_T spectra can be largely absorbed by retuning the initial conditions, starting the transverse expansion later and with lower initial entropy density [30,33], this only acerbates the viscous effects on the elliptic flow v_2, which in this case is further reduced by the decreased fireball lifetime. The reduction of the elliptic flow v_2 by shear viscous effects is therefore a sensitive and robust diagnostic tool for shear viscosity in the fluid [54].

Our results indicate that in semiperipheral Cu + Cu collisions, even a "minimal" amount of shear viscosity [18] causes a reduction of v_2 by almost 50% relative to ideal fluid dynamical simulations. In the present paper, we explored the origin of this reduction in great detail. The effects observed by us for Cu + Cu collisions [36] are larger than those recently reported in Refs. [35,37] for Au + Au collisions. While some of these differences can be attributed to an increased importance of viscous effects in smaller systems, the bulk of the difference appears to arise from the fact that the different groups solve somewhat different sets of viscous hydrodynamic equations [41,55]. (See also the recent interesting suggestion by Pratt [56] for a phenomenological modification of the Israel-Stewart equations for systems with large velocity gradients.) This raises serious questions: if theoretical ambiguities in the derivation of the viscous hydrodynamic equations reflect themselves in large variations of the predicted elliptic flow, any value of the QGP shear viscosity extracted from relativistic heavy-ion data will strongly depend on the specific hydrodynamic model used in the comparison. A reliable quantitative extraction of η/s from experimental data will thus only be possible if these ambiguities can be resolved.

Our studies show that shear viscous effects are strongest during the early stage of the expansion phase when the longitudinal expansion rate is largest. At later times, the viscous corrections become small, although not negligible. Small nonzero viscous pressure components along the hadronic decoupling surface have significant effects on the final hadron spectra that grow with transverse momentum and thus limit the applicability of the viscous hydrodynamic calculation to transverse momenta below 2–3 GeV/c, depending on impact parameter, collision energy, and particle mass. Viscous effects are more important in peripheral than in central collisions, and larger for light than for heavy particles. They increase with the kinetic relaxation time for the viscous pressure tensor. Since the breakdown of viscous hydrodynamics is signaled by the theory itself, through the relative magnitude of the viscous pressure, the applicability of the theory can be checked quantitatively case by case and during each stage of the expansion.

For the kinetic relaxation times τ_π considered in the present work, sensitivities to the initial value of the viscous pressure tensor were found to be small and practically negligible. Sensitivity to the value of τ_π was found for the hadron spectra, especially the elliptic flow, at large transverse momenta. This leads us to suggest restricting any comparison between theory and experiment with the goal of extracting the shear viscosity η/s to the region $p_T \lesssim 1$ GeV/c where the sensitivity to τ_π is sufficiently weak.

The dynamical analysis of shear viscous effects on the momentum anisotropy and elliptic flow in noncentral collisions reveals an interesting feature: the total momentum anisotropy receives two types of contributions, the first resulting from the anisotropy of the collective flow pattern and the second arising from a local momentum anisotropy of the phase-space distribution function in the local fluid rest frame, reflecting viscous corrections to its local thermal equilibrium form. During the early expansion stage, the latter effect (i.e., the fact that large viscous pressure effects generate momentum anisotropies in the local fluid rest frame) dominates the viscous effects on elliptic flow. At later times, these local momentum anisotropies get transferred to the collective flow profile, manifesting themselves as a viscous reduction of the collective flow anisotropy. The time scale for transferring the viscous correction to v_2 from the local rest frame momentum distribution to the collective flow pattern appears to be of the same order as that for the evolution of the total momentum anisotropy itself.

Several additional steps are necessary before the work presented here can be used as a basis for a quantitative interpretation of relativistic heavy-ion data. First, the above-mentioned ambiguity of the detailed form of the kinetic evolution equations for the viscous pressure must be resolved. Second, the equation of state must be fine-tuned to lattice QCD data and other available information to make it as realistic as presently possible. The hydrodynamic scaling of the final elliptic flow v_2 with the initial source eccentricity ϵ_x [57] and its possible violation by viscous effects need to be explored [41], in order to assess the sensitivity of the scaled elliptic flow v_2/ϵ_x to details of the model used for initializing the hydrodynamic evolution [13]. The temperature dependence of the specific shear viscosity η/s, especially across the quark-hadron phase transition [52,53], must be taken into account, and bulk viscous effects, again particularly near T_c, must be included. To properly account for the highly viscous nature of the hadron resonance gas during the last collision stage, it may be necessary to match the viscous hydrodynamic formalism to a microscopic hadronic cascade to describe the last part of the expansion until hadronic decoupling [52]. We expect to report soon on progress along some of these fronts.

Note added. Just before submitting this work for publication we became aware of Ref. [60], in which the form of the kinetic

evolution equations for the viscous pressure is revisited and it is argued that Eqs. (4) and (5) must be amended by additional terms that reduce the strong viscous suppression of the elliptic flow observed by us [55]. While details of the numerical results will obviously change if these terms are included (cf. Refs. [35,37]), our discussion of the driving forces behind the finally observed viscous corrections to ideal fluid results and of the evolution of these corrections with time is generic, and the insights gained in the present study are expected to hold, at least qualitatively, also for future improved versions of VISH2+1 that properly take into account the new findings reported in Ref. [60].

ACKNOWLEDGMENTS

The viscous hydrodynamic code VISH2+1 employs several subroutines from AZHYDRO, the (2 + 1)-dimensional ideal hydrodynamic code developed by P. Kolb [39,45], especially the flux-corrected SHASTA transport algorithm [58] for evolving the hydrodynamic equations. We thank R. Baier, E. Frodermann, P. Kolb, S. Pratt, P. Romatschke, D. Teaney, and U. Wiedemann for fruitful discussions. This work was supported by the US Department of Energy under Contract DE-FG02-01ER41190.

APPENDIX A: EXPRESSIONS FOR $\tilde{\pi}^{mn}$ AND $\tilde{\sigma}^{mn}$

The expressions for $\tilde{\pi}^{mn}$ and $\tilde{\sigma}^{mn}$ in Eq. (10) are

$$\tilde{\pi}^{mn} = \begin{pmatrix} \pi^{\tau\tau} & \pi^{\tau x} & \pi^{\tau y} & 0 \\ \pi^{\tau x} & \pi^{xx} & \pi^{xy} & 0 \\ \pi^{\tau y} & \pi^{xy} & \pi^{yy} & 0 \\ 0 & 0 & 0 & \tau^2\pi^{\eta\eta} \end{pmatrix}, \tag{A1}$$

$$\tilde{\sigma}^{mn} = \begin{pmatrix} \partial_\tau u^\tau & \frac{\partial_\tau u^x - \partial_x u^\tau}{2} & \frac{\partial_\tau u^y - \partial_y u^\tau}{2} & 0 \\ \frac{\partial_\tau u^x - \partial_x u^\tau}{2} & -\partial_x u^x & -\frac{\partial_x u^y + \partial_y u^x}{2} & 0 \\ \frac{\partial_\tau u^y - \partial_y u^\tau}{2} & -\frac{\partial_x u^y + \partial_y u^x}{2} & -\partial_y u^y & 0 \\ 0 & 0 & 0 & -\frac{u^\tau}{\tau} \end{pmatrix}$$

$$- \frac{1}{2} \begin{pmatrix} D((u^\tau)^2) & D(u^\tau u^x) & D(u^\tau u^y) & 0 \\ D(u^\tau u^x) & D((u^x)^2) & D(u^x u^y) & 0 \\ D(u^\tau u^y) & D(u^x u^y) & D((u^y)^2) & 0 \\ 0 & 0 & 0 & 0 \end{pmatrix}$$

$$+ \frac{1}{3}(\partial \cdot u) \begin{pmatrix} (u^\tau)^2 - 1 & u^\tau u^x & u^\tau u^y & 0 \\ u^\tau u^x & (u^x)^2 + 1 & u^x u^y & 0 \\ u^\tau u^y & u^x u^y & (u^y)^2 + 1 & 0 \\ 0 & 0 & 0 & 1 \end{pmatrix}. \tag{A2}$$

Here $D = u^\tau \partial_\tau + u^x \partial_x + u^y \partial_y$ and $\partial \cdot u = \partial_\tau u^\tau + \partial_x u^x + \partial_y u^y + \frac{u^\tau}{\tau}$.

APPENDIX B: VELOCITY FINDING

As shown in Ref. [27], since we evolve all three components $\pi^{\tau\tau}$, $\pi^{\tau x}$, and $\pi^{\tau y}$ (one of which is redundant because of the constraint $\pi^{\tau m} u_m = 0$), the flow velocity and energy density can be found from the energy-momentum tensor components with the same efficient one-dimensional zero-search algorithm employed in ideal hydrodynamics [59]. This is important since this step has to be performed after each time step at all spatial grid points in order to evaluate the EOS $p(e)$.

Using the output from the numerical transport algorithm, one defines the two-dimensional vector $\boldsymbol{M} = (M_x, M_y) \equiv (T^{\tau x} - \pi^{\tau x}, T^{\tau y} - \pi^{\tau y})$. This is the ideal fluid part of the transverse momentum density vector; as such it is parallel to the transverse flow velocity $\boldsymbol{v}_\perp = (v_x, v_y)$. Introducing further $M_0 \equiv T^{\tau\tau} - \pi^{\tau\tau}$, one can write the energy density as

$$e = M_0 - \boldsymbol{v}_\perp \cdot \boldsymbol{M} = M_0 - v_\perp M, \tag{B1}$$

where $v_\perp = \sqrt{v_x^2 + v_y^2}$ is the transverse flow speed and $M \equiv \sqrt{M_x^2 + M_y^2}$. One sees that solving for e requires only the magnitude of $\boldsymbol{v}_\perp$ which is obtained by solving the implicit relation [27,59]

$$v_\perp = \frac{M}{M_0 + p(e = M_0 - v_\perp M)} \tag{B2}$$

by a one-dimensional zero-search. The flow velocity components are then reconstructed using

$$v_x = v_\perp \frac{M_x}{M}, \quad v_y = v_\perp \frac{M_y}{M}. \tag{B3}$$

Note that this requires direct numerical propagation of all three components ($\pi^{\tau\tau}$, $\pi^{\tau x}$, and $\pi^{\tau y}$) since the flow velocity is not known until after the velocity-finding step has been completed. Hence the transversality constraint $\pi^{\tau m} u_m = 0$ cannot be used to determine, say, $\pi^{\tau\tau}$ from $\pi^{\tau x}$ and $\pi^{\tau y}$. However, it can be used after the fact to test the numerical accuracy of the transport code.

APPENDIX C: π^{mn} IN TRANSVERSE POLAR COORDINATES

Although VISH2+1 uses Cartesian (x, y) coordinates in the transverse plane, polar (r, ϕ) coordinates may be convenient for understanding some of the results in the limit of zero impact parameter where azimuthal symmetry is restored. In (τ, r, ϕ, η) coordinates, the flow velocity takes the form $u^m = \gamma_\perp(1, v_r, v_\phi, 0)$, with $\gamma_\perp = 1/\sqrt{1 - v_\perp^2} = 1/\sqrt{1 - v_r^2 - r^2 v_\phi^2}$. The polar coordinate components of the shear pressure tensor components π^{mn} are obtained from those in (τ, x, y, η) coordinates by the transformations

$$\begin{aligned} \pi^{\tau r} &= \pi^{\tau x}\cos\phi + \pi^{\tau y}\sin\phi, \\ r\pi^{\tau\phi} &= -\pi^{\tau x}\sin\phi + \pi^{\tau y}\cos\phi, \\ \pi^{rr} &= \pi^{xx}\cos^2\phi + 2\pi^{xy}\sin\phi\cos\phi + \pi^{yy}\sin^2\phi, \\ r^2\pi^{\phi\phi} &= \pi^{xx}\sin^2\phi - 2\pi^{xy}\sin\phi\cos\phi + \pi^{yy}\cos^2\phi, \\ r\pi^{r\phi} &= (\pi^{yy} - \pi^{xx})\sin\phi\cos\phi + \pi^{xy}(\cos^2\phi - \sin^2\phi), \end{aligned} \tag{C1}$$

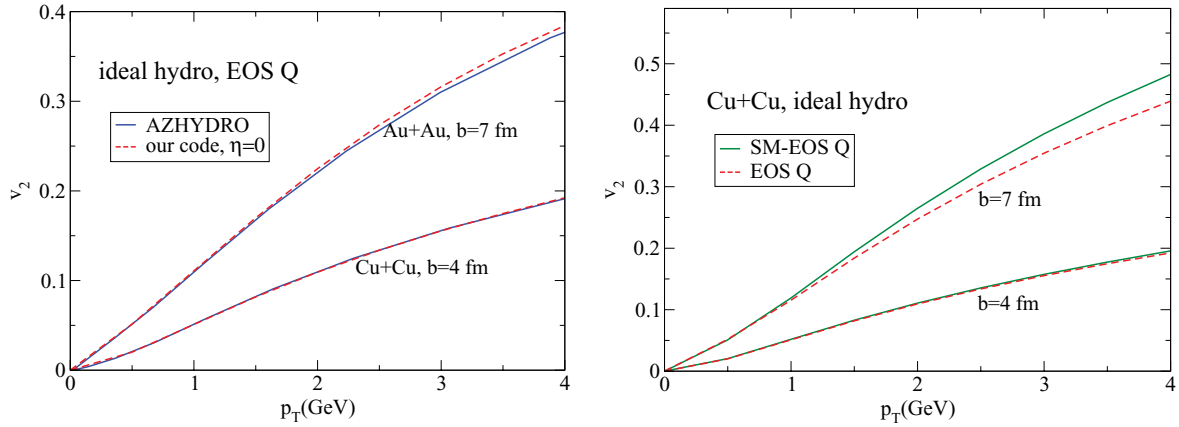

FIG. 22. (Color online) Left: Differential elliptic flow $v_2(p_T)$ for π^- from $b = 4$ fm Cu + Cu collisions and $b = 7$ fm Au + Au collisions, using EOS Q. Results from VISH2+1 for $\eta = 0$ and $\pi^{mn} = 0$ are compared with the ideal fluid code AZHYDRO. Right: $v_2(p_T)$ for π^- from Cu + Cu collisions at impact parameters $b = 4$ and 7 fm, comparing VISH2+1 evolution with EOS Q and SM-EOS Q in the ideal fluid limit $\eta = 0, \pi^{mn} = 0$.

with $\cos\phi = x/r$ and $\sin\phi = y/r$. In terms of these, the independent components Σ and Δ of Eqs. (19) and (20) are given as

$$\begin{aligned} \Sigma &= \pi^{rr} + r^2\pi^{\phi\phi}, \\ \Delta &= \cos(2\phi)(\pi^{rr} - r^2\pi^{\phi\phi}) - 2\sin(2\phi)\, r\pi^{r\phi}, \end{aligned} \tag{C2}$$

from which we easily get

$$\begin{aligned} 2\pi^{xx} &= \pi^{rr}(1 + \cos(2\phi)) + r^2\pi^{\phi\phi}(1 - \cos(2\phi)), \\ 2\pi^{yy} &= \pi^{rr}(1 - \cos(2\phi)) + r^2\pi^{\phi\phi}(1 + \cos(2\phi)). \end{aligned} \tag{C3}$$

Note that azimuthal symmetry at $b = 0$ implies $\pi^{r\phi} = 0$ and a vanishing azimuthal average for Δ, that is, $\langle\Delta\rangle_\phi = 0$ or $\langle\pi^{xx}\rangle_\phi = \langle\pi^{yy}\rangle_\phi$.

APPENDIX D: TESTS OF THE VISCOUS HYDRODYNAMIC CODE VISH2+1

A. Testing the ideal hydrodynamic part of VISH2+1

When one sets $\pi^{mn} = 0$ initially and takes the limit $\eta = 0$, VISH2+1 simulates the evolution of an ideal fluid, and its results should agree with those of the well-tested and publicly available (2 + 1)-dimensional ideal fluid code AZHYDRO [39]. Since VISH2+1 was written independently, using only the flux-corrected SHASTA transport algorithm from the AZHYDRO package [39,58] in its evolution part, this is a useful test of the code. The left panel in Fig. 22 shows that for identical initial and final conditions as described in Sec. II, the two codes indeed produce almost identical results. The small difference in the Au+Au system at $b = 7$ fm is likely due to the slightly better accuracy of AZHYDRO, which, in contrast to VISH2+1, invokes an additional time-splitting step in its evolution algorithm.

When comparing our VISH2+1 results with AZHYDRO, we initially found somewhat larger discrepancies which, however, could be traced back to different versions of the EOS used in the codes: EOS Q in AZHYDRO, the smoothed version SM-EOS Q in VISH2+1. In the left panel of Fig. 22, this difference has been removed, by running also VISH2+1 with EOS Q. In the right panel, we compare VISH2+1 results for EOS Q and for SM-EOS Q, showing that even the tiny rounding effects resulting from the smoothing procedure used in SM-EOS Q (which renders the EOS slightly stiffer in the mixed phase) lead to differences in the elliptic flow for peripheral collisions of small nuclei which exceed the numerical error of the code.

B. Comparison with analytical results for (0 + 1)-d boost-invariant viscous hydro

For boost-invariant longitudinal expansion without transverse flow, the relativistic Navier-Stokes equations read [16]

$$\frac{\partial e}{\partial \tau} + \frac{e + p + \tau^2\pi^{\eta\eta}}{\tau} = 0, \tag{D1}$$

$$\tau^2\pi^{\eta\eta} = -\frac{4}{3}\frac{\eta}{\tau}. \tag{D2}$$

For an ideal gas EOS $p = \frac{1}{3}e \sim T^4$ this leads to the following analytic solution for the temperature evolution [16]:

$$\frac{T(\tau)}{T_0} = \left(\frac{\tau_0}{\tau}\right)^{1/3}\left[1 + \frac{2\eta}{3s\tau_0 T_0}\left(1 - \left(\frac{\tau_0}{\tau}\right)^{2/3}\right)\right]. \tag{D3}$$

To test our code against this analytical result, we initialize VISH2+1 with homogeneous transverse density distributions (not transverse pressure gradients and flow) and use the Navier-Stokes identification $\pi^{mn} = 2\eta\sigma^{mn}$ in the hydrodynamic part of the evolution algorithm, sidestepping the part of the code that evolves π^{mn} kinetically. It turns out that in this case, the relativistic Navier-Stokes evolution is numerically stable. Figure 23 compares the numerically computed temperature evolution from VISH2+1 with the analytic formula (D3), for $\eta/s = 0.08$ and $T_0 = 360$ MeV at $\tau_0 = 0.6$ fm/c. They agree perfectly.

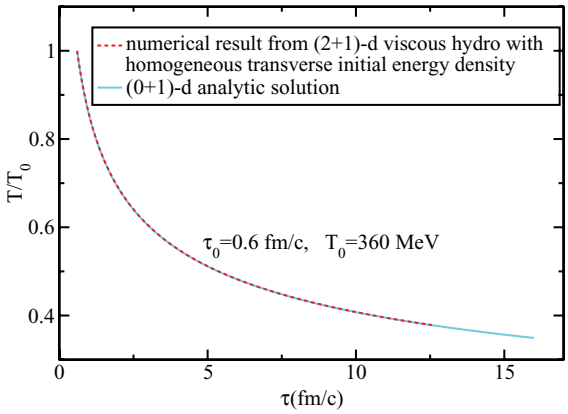

FIG. 23. (Color online) Comparison between the analytical temperature evolution for (0 + 1)-d boost-invariant Navier-Stokes viscous hydrodynamics and numerical results from VISH2+1 with homogeneous transverse initial energy density profiles.

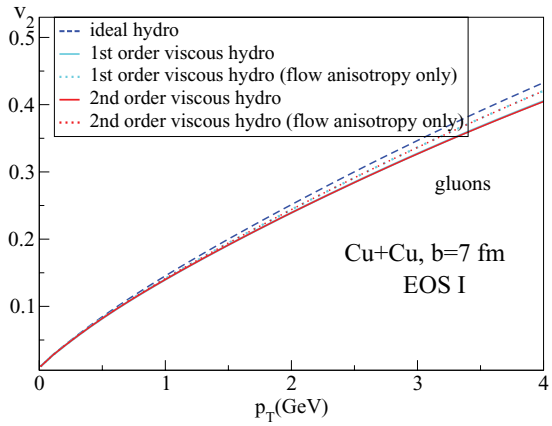

FIG. 24. (Color online) Differential elliptic flow $v_2(p_T)$ for gluons from $b = 7$ fm Cu + Cu collisions, calculated with ideal hydrodynamics, relativistic Navier-Stokes (NS) hydrodynamics, and Israel-Stewart (IS) viscous hydrodynamics with $\frac{\eta}{s} = \frac{T}{2\,\mathrm{GeV}}$ and $\tau_\pi = 0.03$ fm/c, using EOS I. The lines for NS and IS viscous hydrodynamics are almost indistinguishable. Solid lines show the full results from viscous hydrodynamics, dotted lines neglect viscous corrections to the spectra and take only the flow anisotropy effect into account.

C. Reduction of VISH2+1 to relativistic Navier-Stokes theory for small η and τ_π

Having tested the hydrodynamic part of the evolution algorithm in Appendix D 1, we would like to demonstrate also the accuracy of the kinetic evolution algorithm that evolves the viscous pressure tensor components. A straightforward approach would be to take VISH2+1, set the relaxation time τ_π as close to zero as possible, and compare the result with a similar calculation as in Appendix D 1 in which we sidestep the kinetic evolution algorithm and instead insert directly into the hydrodynamic evolution code the Navier-Stokes identity $\pi^{mn} = 2\eta\sigma^{mn}$. Unfortunately, this naive procedure exposes us to the well-known instability and acausality problems of the relativistic Navier-Stokes equations. The suggested procedure only works if a set of initial conditions and transport coefficients can be found where these instabilities do not kick in before the freeze-out surface has been reached.

We found that sufficiently stable evolution of the relativistic Navier-Stokes algorithm (i.e., of VISH2+1 with the identification $\pi^{mn} = 2\eta\sigma^{mn}$) can be achieved for standard initial density profiles in Cu + Cu collisions and the simple ideal gas equation of state EOS I by choosing a very small and temperature-dependent specific shear viscosity $\frac{\eta}{s} = 0.01\,\frac{T}{200\,\mathrm{MeV}} = \frac{T}{2\,\mathrm{GeV}}$. For the Israel-Stewart evolution, we use a relaxation time that is correspondingly short: $\tau_\pi = \frac{3\eta}{sT} = 0.03$ fm/c.

Figure 24 shows the differential elliptic flow $v_2(p_T)$ for gluons in $b = 7$ fm Cu + Cu collisions evolved with these parameters. The dashed line gives the ideal fluid result. The solid and dotted lines show the total elliptic flow and the anisotropic flow contribution to $v_2(p_T)$, respectively, similar to the left panel in Fig. 12. There are two solid and dotted lines with different colors, corresponding to Israel-Stewart and Navier-Stokes evolution; they are indistinguishable, but clearly different from the ideal fluid result. We conclude that for small shear viscosity η/s and in the limit $\tau_\pi \to 0$, the second-order Israel-Stewart algorithm reproduces the Navier-Stokes limit and that, therefore, VISH2+1 evolves the kinetic equations for π^{mn} accurately.

APPENDIX E: HYDRODYNAMICS VS BLAST WAVE MODEL

As discussed in Sec. III B, the viscous corrections to the final pion spectra from the hydrodynamic model have a different sign (at least in the region $p_T > 1$ GeV) than those originally obtained by Teaney [15]. In this Appendix we try to explore the origins of this discrepancy. We will see that the sign and magnitude of viscous corrections to the (azimuthally averaged) particle spectra are fragile and depend on details of the dynamical evolution and hydrodynamic properties on the freeze-out surface. Fortunately, the same caveat does not seem to apply to the viscous corrections to elliptic flow where hydrodynamic and blast wave model calculations give qualitatively similar answers.

Following Teaney's procedure, we calculate π^{mn} in the Navier-Stokes limit $\pi^{mn} = 2\eta\sigma^{mn}$. We do this both in the blast wave model and using the results for σ^{mn} from VISH2+1. For the blast wave model, we assume, as Teaney did, freeze-out at constant τ with a boxlike density profile $e(r) = e_{\mathrm{dec}}\theta(R_0 - r)$, where $e_{\mathrm{dec}} = 0.085\,\mathrm{GeV/fm}^3$ is the same freeze-out energy density as in the hydrodynamic model for EOS I, and $R_0 = 6$ fm. The velocity profile in the blast wave model is taken to be linear, $u_r(r) = a_0\frac{r}{R_0}\theta(R_0 - r)$, with $a_0 = 0.5$; freeze-out is assumed to occur at $\tau_{\mathrm{dec}} = 4.1$ fm/c. R_0, a_0, and τ_{dec} are somewhat smaller than in Ref. [15] since we study Cu + Cu instead of Au + Au collisions. We concentrate here on a discussion of π^{rr} for illustration; the expression for σ^{rr} is found in Ref. [27], Eq. (A11c). While π^{rr} from VISH2+1 differs from $2\eta\sigma^{rr}$ because of the finite relaxation time τ_π (see

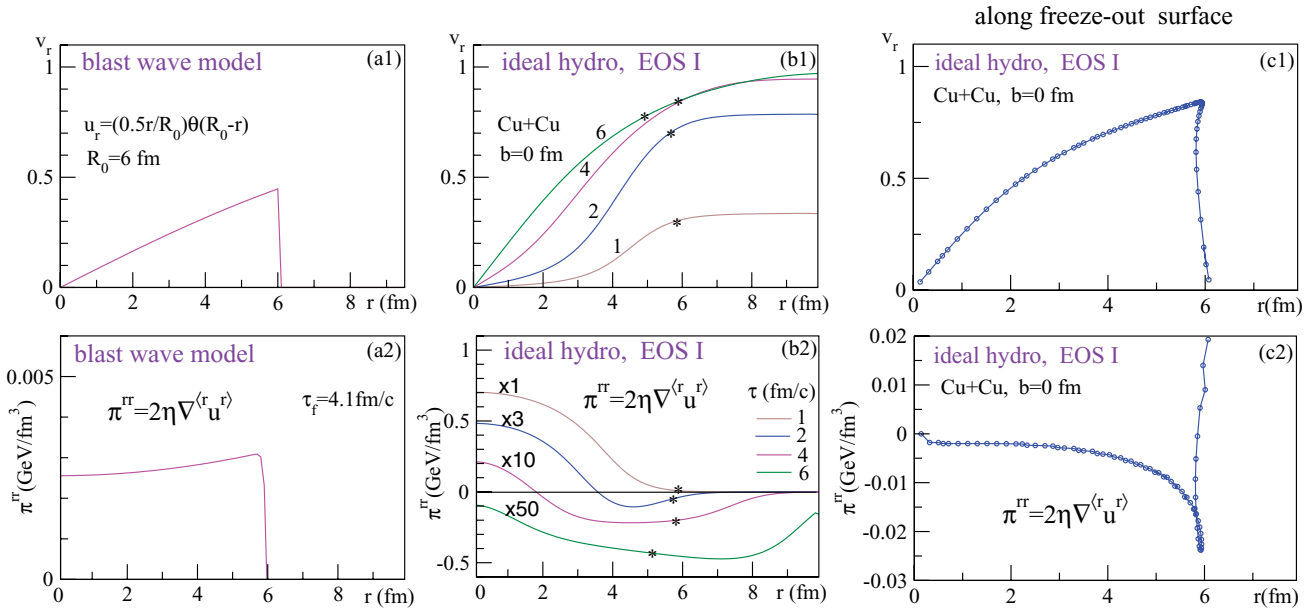

FIG. 25. (Color online) Top row: Velocity profiles from the blast wave model (left) and from the hydrodynamic model with EOS I at fixed times (middle) and along the decoupling surface (right). Bottom row: The corresponding profiles for the transverse shear viscous pressure π^{rr} in the Navier-Stokes limit, $\pi^{rr} = 2\eta\nabla^{\langle\mu}u^{\nu\rangle}$. Calculations are for central Cu + Cu collisions, and the curves in the middle panels correspond to the times $\tau = 1, 2, 4$, and 6 fm/c.

Sec. V C), we have checked that the signs of these two quantities are the same on the freeze-out surface so that our discussion provides at least a qualitatively correct analysis of the viscous spectra corrections in the two models.

In Fig. 25, we compare the freeze-out profiles for the radial flow velocity and $2\eta\sigma^{rr}$ from the blast wave model. In spite of the qualitative similarity of the velocity profiles, the freeze-out profiles of $2\eta\sigma^{rr}$ are entirely different and even have the opposite sign in the region where most of the hydrodynamic particle production occurs (left and right columns in Fig. 25). The middle column shows that at fixed times τ, the hydrodynamic profile for $2\eta\sigma^{rr}$ shows some similarity with the blast wave model in that $2\eta\sigma^{rr}$ is positive throughout most of the interior of the fireball. What matters for the calculation of the spectra via Eq. (12), however, are the values of $2\eta\sigma^{rr}$ on the freeze-out surface Σ where they are negative, mostly because of radial velocity derivatives. This explains the opposite sign of the viscous correction to the spectra in the hydrodynamic model and shows that as far as an estimate of these viscous corrections goes, the blast wave model has serious limitations.

[1] P. F. Kolb and U. Heinz, in *Quark-Gluon Plasma 3*, edited by R. C. Hwa and X.-N. Wang (World Scientific, Singapore, 2004), p. 634 (arXiv: nucl-th/0305084).
[2] U. Heinz and P. F. Kolb, Nucl. Phys. **A702**, 269 (2002).
[3] M. Gyulassy, in *Structure and Dynamics of Elementary Matter*, edited by W. Greiner *et al.*, NATO Sci. Ser. II: Mathematics, Physics and Chemistry, Vol. 166 (Kluwer Academic, Dordrecht, 2004), p. 159 (arXiv: nucl-th/0403032).
[4] M. Gyulassy and L. McLerran, Nucl. Phys. **A750**, 30 (2005).
[5] E. V. Shuryak, Nucl. Phys. **A750**, 64 (2005).
[6] P. Huovinen, arXiv:0710.4379 [nucl-th].
[7] J. Berges, S. Borsanyi, and C. Wetterich, Phys. Rev. Lett. **93**, 142002 (2004); Nucl. Phys. **B727**, 244 (2005).
[8] S. Mrowczynski, Eur. Phys. J. A **31**, 875 (2007), and references therein.
[9] P. Arnold, J. Lenaghan, G. D. Moore, and L. G. Yaffe, Phys. Rev. Lett. **94**, 072302 (2005); P. Arnold, G. D. Moore, and L. G. Yaffe, Phys. Rev. D **72**, 054003 (2005); P. Arnold and G. D. Moore, *ibid.* **73**, 025006 (2006); **73**, 015013 (2006).
[10] M. Strickland, J. Phys. G: Nucl. Part. Phys. **34**, S429 (2007), and references therein.
[11] Y. V. Kovchegov and A. Taliotis, Phys. Rev. C **76**, 014905 (2007).
[12] U. Heinz, J. Phys. G: Nucl. Part. Phys. **31**, S717 (2005).
[13] T. Hirano, U. Heinz, D. Kharzeev, R. Lacey, and Y. Nara, Phys. Lett. **B636**, 299 (2006).
[14] D. Molnar and M. Gyulassy, Nucl. Phys. **A697**, 495 (2002); **A703**, 893(E) (2002).
[15] D. Teaney, Phys. Rev. C **68**, 034913 (2003).
[16] P. Danielewicz and M. Gyulassy, Phys. Rev. D **31**, 53 (1985).
[17] G. Policastro, D. T. Son, and A. O. Starinets, Phys. Rev. Lett. **87**, 081601 (2001); J. High Energy Phys. 09 (2002) 043.
[18] P. Kovtun, D. T. Son, and A. O. Starinets, Phys. Rev. Lett. **94**, 111601 (2005).
[19] R. A. Janik, Phys. Rev. Lett. **98**, 022302 (2007).
[20] P. Arnold, G. D. Moore, and L. G. Yaffe, J. High Energy Phys. 11 (2000) 001; 05 (2003) 051.
[21] H. B. Meyer, Phys. Rev. D **76**, 101701 (2007).
[22] M. Asakawa, S. A. Bass, and B. Müller, Phys. Rev. Lett. **96**, 252301 (2006); Prog. Theor. Phys. **116**, 725 (2007).

[23] P. Romatschke, arXiv:0710.0016 [nucl-th].
[24] C. Eckart, Phys. Rev. **58**, 919 (1940).
[25] L. D. Landau and E. M. Lifshitz, *Fluid Mechanics* (Pergamon, Oxford, 1963), Sec. 127.
[26] W. Israel, Ann. Phys. (NY) **100**, 310 (1976); W. Israel and J. M. Stewart, *ibid*. **118**, 341 (1979).
[27] U. Heinz, H. Song, and A. K. Chaudhuri, Phys. Rev. C **73**, 034904 (2006).
[28] A. Muronga, Phys. Rev. Lett. **88**, 062302 (2002); **89**, 159901(E) (2002); Phys. Rev. C **69**, 034903 (2004); **76**, 014909 (2007); **76**, 014910 (2007).
[29] D. A. Teaney, J. Phys. G **30**, S1247 (2004).
[30] R. Baier, P. Romatschke, and U. A. Wiedemann, Phys. Rev. C **73**, 064903 (2006).
[31] A. Muronga and D. H. Rischke, arXiv:nucl-th/0407114.
[32] A. K. Chaudhuri and U. Heinz, J. Phys.: Conf. Ser. **50**, 251 (2006).
[33] R. Baier and P. Romatschke, Eur. Phys. J. C **51**, 677 (2007); P. Romatschke, *ibid*. **52**, 203 (2007).
[34] A. K. Chaudhuri, arXiv:0704.0134 [nucl-th]; arXiv:0708.1252 [nucl-th].
[35] P. Romatschke and U. Romatschke, Phys. Rev. Lett. **99**, 172301 (2007).
[36] H. Song and U. Heinz, Phys. Lett. **B658**, 279 (2008).
[37] K. Dusling and D. Teaney, Phys. Rev. C **77**, 034905 (2008).
[38] A. K. Chaudhuri, Phys. Rev. C **74**, 044904 (2006).
[39] AZHYDRO can be downloaded from URL http://nt3.phys.columbia.edu/people/molnard/OSCAR/.
[40] P. Danielewicz and M. Gyulassy, Phys. Rev. D **31**, 53 (1985).
[41] H. Song and U. Heinz (to be published).
[42] H. B. Meyer, arXiv:0710.3717 [hep-lat].
[43] K. Paech and S. Pratt, Phys. Rev. C **74**, 014901 (2006).
[44] D. Kharzeev and K. Tuchin, arXiv:0705.4280 [hep-ph].
[45] P. F. Kolb, J. Sollfrank, and U. Heinz, Phys. Lett. **B459**, 667 (1999); Phys. Rev. C **62**, 054909 (2000).
[46] A. Dumitru, E. Molnar, and Y. Nara, Phys. Rev. C **76**, 024910 (2007).
[47] F. Cooper and G. Frye, Phys. Rev. D **10**, 186 (1974).
[48] U. Heinz, in *2003 CERN-CLAF School of High-Energy Physics, San Miguel Regla, Mexico 1–14 June 2003*, edited by N. Ellis, CERN Yellow Report CERN-2006-001, p.165 [arXiv:hep-ph/0407360].
[49] J. D. Bjorken, Phys. Rev. D **27**, 140 (1983).
[50] J. Y. Ollitrault, Phys. Rev. D **46**, 229 (1992).
[51] T. Hirano and U. Heinz, unpublished notes.
[52] T. Hirano and M. Gyulassy, Nucl. Phys. **A769**, 71 (2006).
[53] L. P. Csernai, J. I. Kapusta, and L. D. McLerran, Phys. Rev. Lett. **97**, 152303 (2006).
[54] U. Heinz and S. M. H. Wong, Phys. Rev. C **66**, 014907 (2002).
[55] P. Romatschke (private communication).
[56] S. Pratt, Phys. Rev. C **77**, 024910 (2008).
[57] H. Heiselberg and A. M. Levy, Phys. Rev. C **59**, 2716 (1999); S. A. Voloshin and A. M. Poskanzer, Phys. Lett. **B474**, 27 (2000); C. Alt *et al*. (NA49 Collaboration), Phys. Rev. C **68**, 034903 (2003); R. S. Bhalerao, J. P. Blaizot, N. Borghini, and J. Y. Ollitrault, Phys. Lett. **B627**, 49 (2005); R. S. Bhalerao and J. Y. Ollitrault, *ibid*. **B641**, 260 (2006); G. Torrieri, Phys. Rev. C **76**, 024903 (2007); H. J. Drescher, A. Dumitru, C. Gombeaud, and J. Y. Ollitrault, *ibid*. **76**, 024905 (2007).
[58] J. P. Boris and D. L. Book, J. Comput. Phys. **11**, 38 (1973).
[59] D. Rischke, S. Bernard, and J. A. Maruhn, Nucl. Phys. **A595**, 346 (1995).
[60] R. Baier, P. Romatschke, D. T. Son, A. O. Starinets, and M. A. Stephanov, arXiv:0712.2451 [hep-th].